

Aerosol-Induced Changes in Atmospheric and Oceanic Heat Transports in the CESM2 Large Ensemble

MICHAEL R. NEEDHAM ^a, TYLER COX,^b AND DAVID A. RANDALL^a

^a *Department of Atmospheric Science, Colorado State University, Fort Collins, Colorado*

^b *Department of Atmospheric Sciences, University of Washington, Seattle, Washington*

(Manuscript received 28 July 2023, in final form 13 June 2024, accepted 25 July 2024)

ABSTRACT: The total poleward energy transport (PET) is set by the top of atmosphere radiation flux and is therefore sensitive to any process which can alter those fluxes, particularly in the shortwave. One example is the direct and indirect effects of anthropogenic aerosols, which increase the local reflection of solar radiation back into space. The historic emission of sulfur dioxide, which peaked in the northern midlatitudes during the 1980s, has been proposed as a primary contributor to historic anomalies in cross-equatorial energy transport, as well as related processes such as a shift in the tropical rainband. In this study, we analyze simulations from the Community Earth System Model, version 2 (CESM2), large ensemble and single-forcing projects to better understand the forced response of PET to historical forcings. First, analysis of the single-forcing project reveals that the position of the intertropical convergence zone (ITCZ) responds in a nonlinear manner to greenhouse gas forcing in CESM2. This type of nonlinearity has been found previously in the context of the aerosol-only simulations in the CESM2 single-forcing project but may be the first identification of a similar effect in the greenhouse gas-only simulations. Second, through analysis of the full CESM2 large ensemble simulations, we find that anomalous heat transport occurred in both the atmosphere (through the mean meridional circulation and atmospheric eddies) and the oceans (through the Atlantic and Indo-Pacific sectors) due to a variety of related processes including the Hadley cells, the midlatitude storm tracks, the Atlantic meridional overturning circulation (AMOC), and the Pacific wind-driven subtropical gyre.

SIGNIFICANCE STATEMENT: In this study, we investigate how the Earth system changed the transport of energy from the tropics to the poles in response to historic pollution. We analyze a large number of climate model simulations of the recent past (1850 to present) and find that historic emissions of sulfur dioxide caused the model to transport more energy in the form of stronger ocean currents, stronger storms, and stronger prevailing winds. This is because the modeled currents in the Atlantic were too sensitive to historic pollution and transported too much warm water northward.


KEYWORDS: Extratropical cyclones; Hadley circulation; Ocean circulation; Energy transport; Atmosphere-ocean interaction; ENSO


1. Introduction

Virtually every phenomenon of the climate system is ultimately driven by the absorption of radiative energy from the sun and the requirement that the Earth balance this solar heating via the blackbody emission of longwave radiation (Kiehl and Trenberth 1997; Trenberth et al. 2009; von Schuckmann et al. 2016). This balance does not hold instantaneously at each

point but rather holds in an aggregate sense, both spatially and temporally. Observations (Ramanathan 1987; Ramanathan et al. 1989; Loeb et al. 2018) show that the equatorial regions absorb more shortwave energy than they lose to longwave emission, while the opposite is true at the poles. This fact necessitates a poleward energy transport (PET) out of the tropics, of which the vast majority is accomplished by the atmosphere and oceans (Sverdrup 1942; Riehl and Malkus 1958; Bjerknes 1964; Oort 1971; Vonder Haar and Oort 1973; Trenberth 1979; Held 2001; Trenberth and Stepaniak 2004; Czaja and Marshall 2006). Then, any changes in the spatial pattern of the radiative balance at the top of the atmosphere imply a corresponding change in the PET (Chiang and Bitz 2005; Enderton and Marshall 2009; Rose and Ferreira 2012; Knietzsch et al. 2015; Shaw and Smith 2022; Pearce and Bodas-Salcedo 2023).

In a recent study, Needham and Randall (2023, hereafter NR23) showed that a large ensemble of historical climate simulations (the CESM2-LE; Rodgers et al. 2021) performed with the Community Earth System Model, version 2 (CESM2; Danabasoglu et al. 2020), produced a large positive (i.e., northward) anomaly in the total PET over a wide range of latitudes, primarily between 30°S and 60°N. They found a similar anomaly

 Denotes content that is immediately available upon publication as open access.

 Supplemental information related to this paper is available at the Journals Online website: <https://doi.org/10.1175/JCLI-D-23-0455.s1>.

Needham's current affiliation: U.S. Environmental Protection Agency, Lenexa, Kansas.

Corresponding author: Michael R. Needham, needham.michael@epa.gov

DOI: 10.1175/JCLI-D-23-0455.1

© 2024 American Meteorological Society. This published article is licensed under the terms of the default AMS reuse license. For information regarding reuse of this content and general copyright information, consult the AMS Copyright Policy (www.ametsoc.org/PUBSReuseLicenses).

Brought to you by NOAA Library | Unauthenticated | Downloaded 04/25/25 06:08 PM UTC

in the PET calculated from ERA5 atmospheric reanalysis (Hersbach et al. 2020) with a magnitude somewhat smaller than the ensemble mean from the CESM2-LE but still within the ensemble spread. Their further analysis of the CESM2 single-forcing large ensemble (Simpson et al. 2023) led NR23 to conclude that the anomaly was primarily driven by anthropogenic aerosol emissions, which cooled the Northern Hemisphere relative to the Southern Hemisphere and induced anomalous northward heat transport in both the atmosphere and oceans. Similar energetic changes in response to aerosol forcing have been found in atmosphere/mixed layer ocean GCM simulations (Ming and Ramaswamy 2011), in CMIP3- and CMIP5-generation models (Hwang et al. 2013; Irving et al. 2019; Lembo et al. 2019, and references therein), as well as in a different CMIP6 generation model (Yukimoto et al. 2022).

These types of energetic changes are known to impact various aspects of the climate system. For example, as a part of the broader body of literature on the energetic theory (Chiang and Bitz 2005; Kang et al. 2008; Marshall et al. 2014; Frierson et al. 2013; Schneider et al. 2014; Adam et al. 2016; Donohoe and Voigt 2017; Kang 2020; Yukimoto et al. 2022) of the position of the intertropical convergence zone (ITCZ), Hwang et al. (2013) analyzed the southward shift of the ITCZ during the latter half of the twentieth century in response to aerosol forcing in the Northern Hemisphere. They proposed a mechanism where an anomalous Hadley circulation was induced that increased the cross-equatorial heat transport in order to balance the aerosol cooling of the Northern Hemisphere.

In this study, we build on the analysis of NR23 to answer the immediate question of how modeled fluid flows in the CESM2-LE changed in the oceans and atmosphere to accomplish the anomalous heat transport indicated by the TOA energy balance. Additionally, we use this energetic framework to uncover a novel example of a change in a CESM2 single-forcing (CESM2-SF) subensemble which does not extend to the simulations forced by all inputs: we find that the change in atmospheric heat transport due only to greenhouse gases leads to a shift in the ITCZ which further analysis indicates is absent from the full CESM2-LE. We also hope this study demonstrates that this type of unified energetic framework is an efficient way to generate testable hypotheses on how some forcing may impact various aspects of the climate system.

2. Methods

a. Data

As in NR23, we primarily analyze the historical (1850–2014) simulations of the CESM2 large ensemble (Rodgers et al. 2021), which includes 100 ensemble members driven by the same anthropogenic aerosol, greenhouse gas, and other forcing datasets used in the CMIP6 (Eyring et al. 2016). The exception is for biomass burning (BMB): 50 of the ensemble members use the CMIP6 BMB forcing dataset, while the remaining 50 members use a smoothed BMB forcing dataset. The smoothed dataset is used to avoid the discontinuity in the CMIP6 BMB field associated with including satellite monitoring

of wildfires (1997–2014; Fasullo et al. 2022). Therefore, the analysis that follows uses the 50 ensemble members with smoothed BMB forcing, unless otherwise noted. Additionally, we analyze output from the CESM2 single-forcing large ensemble (CESM2-SF; Simpson et al. 2023) which is described in full in section 3. Finally, we briefly analyze a long 2000-yr preindustrial control simulation (Danabasoglu et al. 2020) performed with CESM2 for the purpose of investigating the link between El Niño–Southern Oscillation (ENSO) variability and heat transport anomalies in the Indo-Pacific in the absence of changes in external forcings.

Primary postprocessing of model outputs was performed using Python with extensive use of the xarray package (Hoyer and Hamman 2017) for calculations utilizing data from netCDF files. Additionally, TempestExtremes v2.1 (Ullrich et al. 2021) was used to identify trajectories of extratropical cyclones in section 5.

b. Calculation of poleward energy transport

We use the same oceanic heat transport fields as NR23: the CESM2 monthly mean ocean model field “N_HEAT” is read directly from model output files to retrieve the global zonally integrated ocean heat transport and the zonally integrated ocean heat transport in the Atlantic basin. The Indo-Pacific heat transport is then calculated as the difference between the total and Atlantic heat transports at each latitude. The separation between ocean basins becomes ambiguous south of the African continent, so Atlantic and Indo-Pacific heat transports are only shown north of 35°S.

The method used to calculate the atmospheric heat transports, however, is different than that used by NR23. NR23 used an energetic method to calculate the atmospheric heat transport from a polar cap integral of the net TOA minus surface energy balance. This method relied on the assumption of no long-term heat uptake in the atmosphere, which was deemed to be valid on time scales longer than a year. However, this effectively lowered the temporal resolution and only allowed for analysis of the annual mean atmospheric heat transport for any given simulation.

To analyze seasonal rather than annual means and to decompose the heat transport into contributions from the mean meridional circulation (MMC) and from eddies, we require heat transport on monthly time scales. Therefore, we analyze the atmospheric heat transport in the CESM2 large ensemble calculated using the dynamic method described in Cox et al. (2022), alongside calculations of the atmospheric overturning streamfunction.

With the dynamic method, the atmospheric heat transport is calculated by vertically integrating the meridional advection of moist static energy (MSE, i.e., vh for $h = c_p T + gz + L_v q$) at each model grid point and for each time step. This method also allows for the explicit separation of the MSE transport into contributions from the mean meridional circulation and from eddies. For further discussion on the difference between the energetic and dynamic methods, see Armour et al. (2019).

As in NR23, heat transport anomalies are defined so that a positive value indicates anomalous northward transport.

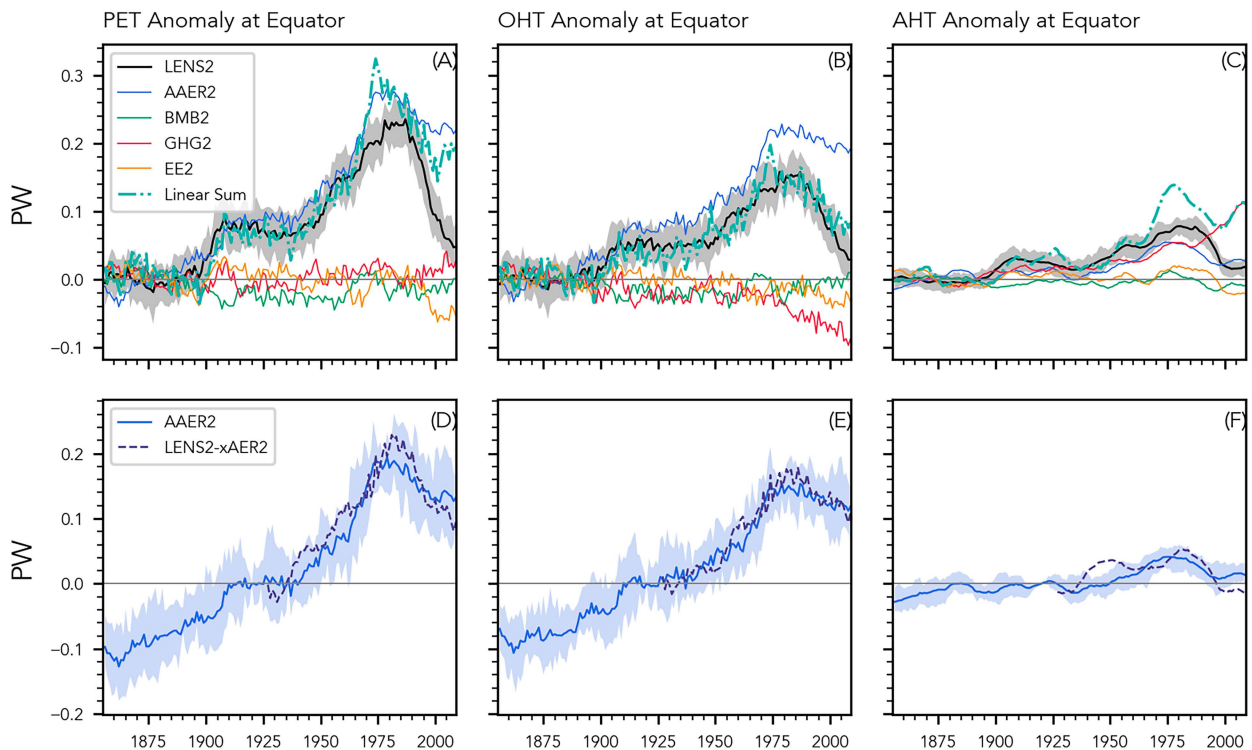


FIG. 1. (a) Anomaly in PET at the equator from the CESM2-LE and CESM2-SF subensembles, alongside the linear sum from the CESM2-SF subensemble means (dashed line, composed of the sum of the AAER2, BMB2, EE2, and GHG2 subensemble means). (b),(c) Oceanic and atmospheric components, respectively, which add together to give the total PET anomaly in (a). (d)–(f) As in (a)–(c), but for the CESM2-SF only-aerosol and all-but-aerosol subensembles (AAER2 and LENS2 minus xAER2, respectively). The shading indicates the interquartile range among ensemble members.

3. Attribution of heat transport changes

NR23 attributed the anomaly in the total poleward energy transport entirely to anthropogenic aerosol forcing. Is the same true for the oceanic and atmospheric components of the energy transport? To answer this question, we analyze simulations from the CESM2 single-forcing large ensemble (Simpson et al. 2023) using atmospheric and oceanic heat transport fields which were originally calculated by NR23. Briefly, these simulations were performed with all forcings held fixed at preindustrial levels except for the forcing of interest (e.g., greenhouse gases) which was allowed to evolve in time. The forcings are greenhouse gases (GHG2; 15 members), anthropogenic aerosols (AAER2; 20 members), biomass burning (BMB2; 15 members), and everything else (EE2; 15 members). An additional “all-but-aerosol” subensemble (xAER2; 10 members) was performed in which all forcings were allowed to evolve in time except for the aerosol forcing, which was fixed at preindustrial levels. This configuration is similar to the configuration of the original CESM1 single-forcing large ensemble (Deser et al. 2020), which utilized this “all-but-one” approach for each of the forcings.

Figures 1a–c show the total, oceanic, and atmospheric heat transport anomaly at the equator for the CESM2-LE (black curve) and for the subensemble means from CESM2-SF. At first glance, Figs. 1b and 1c would appear to refute the claim

that aerosols are the primary drivers of both ocean heat transport (OHT) and atmospheric heat transport (AHT) contributions to the PET. Specifically, we see that the anomaly in the cross-equatorial AHT and OHT due to GHG2 (red curve) is similar in magnitude to the curve for the cross-equatorial AHT anomaly due to AAER2 (blue curve). This indicates that greenhouse gas forcing leads to an anomaly in both the oceanic and atmospheric components in the GHG2 simulations.

However, these plots require careful consideration to be interpreted correctly: a key conclusion of Simpson et al. (2023) is that the “only-one” experimental setup of the AAER2 simulations leads to different results in quantifying the impact of aerosols on CESM2 compared to the all-but-one approach (i.e., the xAER2 simulations). The plots in the top row of Fig. 1 indicate that a similar dynamic occurs with the GHG-only simulations which, to our knowledge, have not been previously discussed in the literature.

To explain this dynamic, we first note that the red curve in Fig. 1a is largely flat which indicates essentially no change in the total poleward energy transport in the GHG2 simulations. This is unsurprising as the theory (Stone 1978) indicates that the total PET can only be altered by changes in the meridional gradient of the TOA radiative flux. Historic anthropogenic aerosol forcing was primarily confined to the region between 30° and 60°N although during the twenty-first century, aerosol emissions have primarily shifted to East and

South Asia (Hoesly et al. 2018). This contrasts with greenhouse gases, which are known to be well-mixed within the atmosphere. Consequently, the direct radiative effect of greenhouse gases cannot lead to a large hemispheric asymmetry in the TOA radiative flux, as is found from the anthropogenic aerosol forcing. It is still conceivable that some forced response to greenhouse gases could impact the hemispheric energy gradient although, from Fig. 1a, this does not appear to be the case in the GHG2 simulations.

Second, we note also that the linear sum (dashed line in Figs. 1a–c) of the subensemble mean heat transport from the GHG2, BMB2, EE2, and AAER2 simulations *diverges* from the large ensembles (LENS2) heat transport due to the atmospheric component in Fig. 1c. This finding is the key point of this discussion as it indicates that the linear combination of the isolated effects of the individual CESM2-SF subensembles cannot explain changes in AHT circa 1975. Furthermore, it is then impossible to attribute the discrepancy in the AHT anomaly to a particular forcing without additional analysis: there must be an important nonlinear process contributing to the AHT anomaly.

We can investigate (and ultimately reject) one possibility, which is that the same aerosol–cryosphere–albedo feedback discussed by Simpson et al. (2023) may be the cause of this nonlinearity in the AHT response. However, this cannot be the case, as shown in the bottom panels of Fig. 1. These panels demonstrate that the simulations in which only the aerosol forcing evolves in time (AAER2) and the simulations in which all forcings *except* the aerosol forcing evolve in time (xAER2) agree on the change in the PET, OHT, and AHT at the equator relative to the baseline period starting in 1920. Therefore, the nonlinearity seen in Fig. 1c cannot be the result of the aerosol component of the forcing. Instead, the larger value for the AHT anomaly from the linear sum of CESM2-SF simulations (gray line in Fig. 1c) compared to the full CESM2-LE ensemble mean (black line) appears to be primarily due to the GHG subensemble.

With this result in mind, we can now demonstrate a first example of how to utilize changes in the PET to generate hypotheses about how the model responded to changes in external forcings. To begin this process, we note that the cross-equatorial AHT is known to be strongly tied to the position of the ITCZ, as discussed in the introduction. Theory predicts that a relative cooling of the Northern Hemisphere relative to the Southern Hemisphere will tend to shift the mean position of the ITCZ southward. The changes in cross-equatorial AHT in Fig. 1c would then suggest changes in the position of the ITCZ in these various simulations. This can be seen in Fig. 2a for the CESM2-LE and CESM2-SF subensembles. Here, we have identified the annual mean position of the ITCZ as the annual mean latitude of the zonal-mean precipitation maximum. Similar to Fig. 1, the linear sum of the subensemble mean ITCZ position (dashed line in Fig. 1b) diverges from the LENS2 ensemble mean toward the end of the historical period. From Fig. 2c, we find that this cannot be due to the aerosol forcing, as the AAER2 and xAER2 simulations are in agreement, similar to Figs. 1d–f.

The combination of Figs. 1 and 2 acts as an effective vantage point from which to diagnose the ways in which various

phenomena in CESM2 respond to the different forcing configurations. We will first consider the GHG2 simulations and note again that the total PET (red curve in Fig. 1a) is flat, which indicates no change in the interhemispheric energy gradient. The OHT on the other hand is negative, consistent with a weakened Atlantic meridional overturning circulation (AMOC) in these simulations as described by Simpson et al. (2023). By construction, the difference in PET and OHT must equal the AHT: we then observe that the AHT change is of the opposite sign, and we have linked this positive anomaly to the southward shift in the ITCZ in Fig. 2. Taken together, this suggests a mechanism in the GHG2 simulations where greenhouse warming in the absence of other forcings leads to a slowdown of the AMOC (likely due to freshwater runoff from Greenland) with a corresponding southward shift of the ITCZ to ensure energetic balance (e.g., Chiang and Bitz 2005).

To our knowledge, this is the first identification of a nonlinear response of CESM2 to greenhouse gas forcing analogous to the nonlinear response to aerosol forcing described by Simpson et al. (2023). It is possible that this is due to the strongly nonlinear behavior of the AMOC in CESM2 as described by Simpson et al. (2023) and in a recent study by Needham et al. (2024). Unfortunately, this point is difficult to investigate further due to the lack of an “all-but-GHG” set of simulations in the CESM2-SF. This topic clearly warrants further investigation but is outside the scope of the current study. For our purposes here, it is enough to conclude that the apparent influence of GHGs on OHT and AHT (e.g., the red curves in Fig. 1) is limited to the GHG-only simulations of the CESM2-SF large ensemble and does not extend to the full CESM2-LE simulations.

Contrast this with what is seen in the AAER2 simulations: the PET anomaly in this case is certainly not flat, and both the OHT and AHT anomalies are positive. Then, this indicates that the AMOC strengthens rather than weakens, while the ITCZ still shifts southward. In short, the ITCZ and AMOC here work together to balance a third factor, namely, a Northern Hemisphere cooling due to a change in the aerosol forcing. As we shall see, the behavior of the full CESM2-LE simulations much more closely follows that of the AAER2 simulations, with a series of distinct phenomena working together to balance aerosol cooling. We will briefly return to the CESM2 single-forcing simulations in a later section as part of our discussion of changes in extratropical cyclones in response to aerosol forcing. However, the remainder of this study will be primarily focused on changes in the full CESM2 large ensemble.

4. Characterization of atmospheric and oceanic heat transport anomaly

Figure 3 shows the ensemble mean anomaly in the poleward energy transport (northward positive) relative to the 1851–1900 baseline. The top panels are similar to Fig. 9 of NR23 but with the color bar scaled to better show the change in the constituent transports rather than the total transport. Both the OHT and AHT anomalies show a characteristic

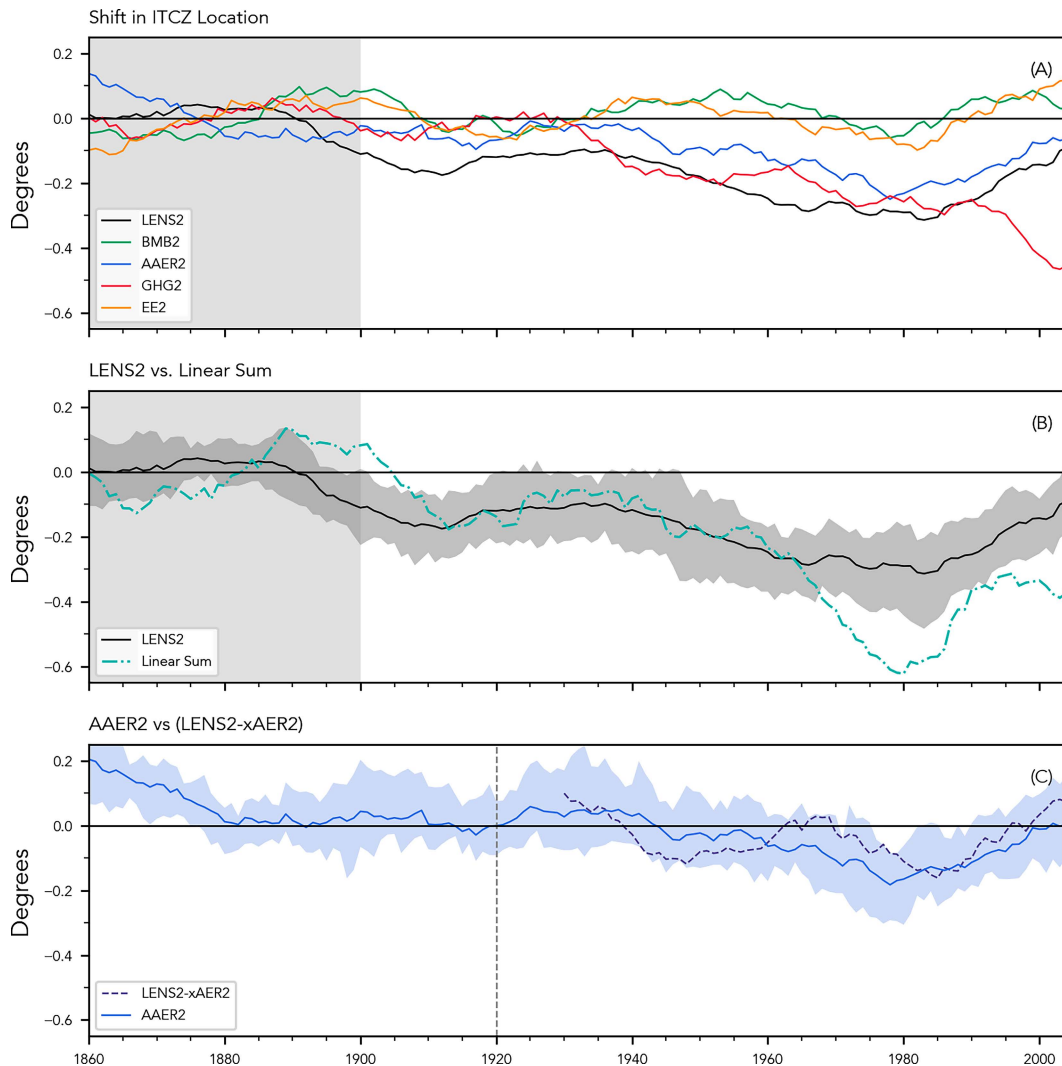


FIG. 2. (a) Shift in the annual mean position of the ITCZ (defined as the annual mean of the monthly mean maximum of the zonal-mean precipitation rate) for the CESM2-LE and for the subensembles of the CESM2-SF project. (b) As in (a), but for comparing the CESM2-LE (with shading showing the interquartile range among the 50 ensemble members) to the linear sum of the subensemble means from the CESM2-SF project (dashed line). (c) As in (a), but for comparing the influence of AAERs on the ITCZ position based on the CESM2-SF only-aerosol and all-but-aerosol subensembles. Note that the influence of aerosols using the xAER2 simulations is found by subtracting the xAER2 ensemble members from the LENS2 ensemble mean.

peak in the latter half of the twentieth century that extends across a wide range of latitudes.

The bottom panels of Fig. 3 show the time average of this anomaly from 1960 to 1989, with the transports further decomposed into contributions from the Atlantic and Indo-Pacific Ocean basins (for OHT) and contributions from the MMC and eddies (for AHT). The shading south of 35°S is included to emphasize that the boundary between the Atlantic and Indo-Pacific Ocean basins becomes ambiguous south of the African continent. The bottom panels show that the maximum OHT anomaly is about twice as large as the maximum AHT anomaly (approximately 0.15 PW vs 0.08 PW), with the largest OHT anomaly found from 15°S to 50°N.

The AHT anomaly is between 0.05 and 0.1 PW from 20°S to 50°N, with the largest values found in the northern midlatitudes. These northern midlatitude values are primarily due to the transient eddy component, while the MMC component dominates in the subtropical regions of both hemispheres. We note that the transient eddy contribution (red curve) is much larger than the contribution from stationary eddies (green curve) in the latitude range of interest. Accordingly, we will omit any further discussion of stationary eddies and henceforth use the term “eddy” with the understanding that this is primarily due to contributions from submonthly transients.

The remainder of this study is devoted to understanding which processes control the anomaly in Atlantic and Indo-Pacific OHT

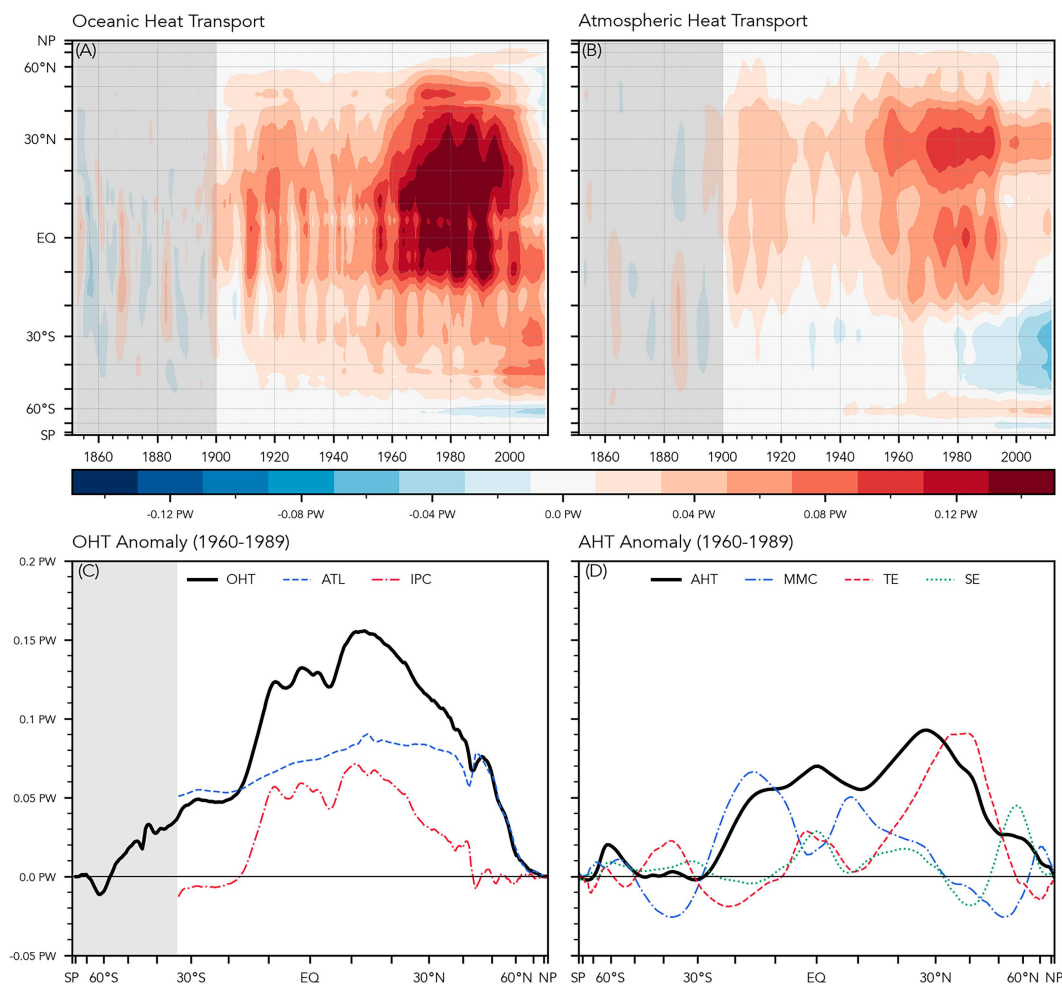


FIG. 3. (top) Anomaly in PET by the (a) oceans and (b) atmosphere relative to the 1851–1900 baseline. (c) Decomposition of total OHT (black) into contributions by the Atlantic (blue, dashed) and Indo-Pacific (red, dash-dotted) basins. (d) Decomposition of total AHT (black) into contributions from the MMC (blue, dash-dotted), transient eddies (red, dashed), and stationary eddies (green, dotted).

(i.e., the bottom-left panel) and the anomaly in MMC and eddy AHT (i.e., the bottom-right panel). We begin by analyzing the AHT anomaly due to the MMC.

5. Decomposition of atmospheric heat transport

a. AHT due to the MMC

The atmospheric MMC from about 30°S to 30°N is dominated by the overturning Hadley cells, which have a distinct seasonal cycle. Accordingly, we begin our decomposition by looking at the seasonal cycle in the AHT anomaly due to the MMC, which is shown in Fig. 4. We first observe that the DJF season has extremely large positive and negative anomalies from 30° to 70°S, but note that these have little impact on the total AHT anomaly because of corresponding and opposite changes in the eddy AHT (as seen in Fig. 6a).

The MMC AHT anomaly has a clear if somewhat muted seasonality: during MAM and especially DJF, there are large

positive anomalies in the Northern Hemisphere from 10° to 30°N. In the Southern Hemisphere, positive anomalies occur during JJA and SON, with somewhat smaller values during MAM. This seasonality suggests a direct link with the Hadley cells. Essentially the anomalous AHT is accomplished by both cells, and the spatial structure (i.e., whether it occurs in the Southern Hemisphere, the Northern Hemisphere, or both) is determined by whether one or both cells is active during a given season.

When we look at the anomaly (1960–89) in the zonal mean meridional streamfunction (Fig. 5), there is a distinct *lack* of seasonality. Instead, we see an anomalous clockwise circulation centered on the equator which changes only slightly with the seasons. This circulation indicates a southward cross-equatorial flux of latent energy and a corresponding northward cross-equatorial flux of dry static energy. As this energy transport by the upper branch is known to be larger than that of the lower branch (Riehl and Malkus 1958; Neelin and Held 1987; Needham and Randall 2021), the net effect is a northward

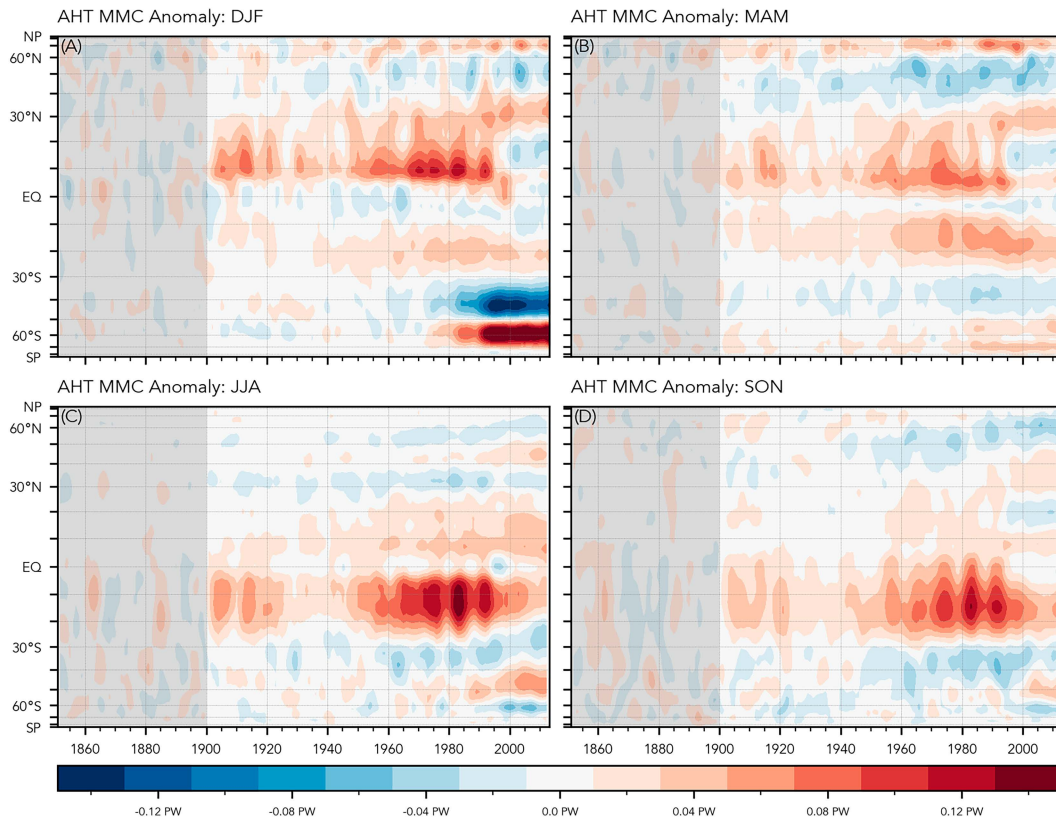


FIG. 4. Ensemble mean anomaly in AHT due to the MMC for each season.

cross-equatorial energy flux by the MMC and a southward shift of the ITCZ, consistent with Fig. 2 and with previous studies (Ming and Ramaswamy 2011; Hwang et al. 2013; Irving et al. 2019; Yukimoto et al. 2022).

b. Changes in extratropical cyclones

We move now to the contribution by eddies to the AHT anomaly (i.e., the red curve in the bottom right panel of Fig. 3). The eddy heat transport has a large peak in the northern mid-latitudes with a maximum value of about 0.1 PW near 40°N. The seasonal decomposition of the AHT eddy anomaly (Fig. 6) shows large anomalies during all seasons except for JJA, with the largest values in DJF and MAM.

The heat transport by eddies is largely accomplished by midlatitude storms in the Atlantic and Pacific storm tracks off the eastern coasts of North America and Japan. These extratropical cyclones (ETCs) grow as a result of atmospheric baroclinicity and act to weaken that baroclinicity through the poleward transport of energy (Hoskins and Valdes 1990; Walker et al. 2020). Then, changes in the frequency or intensity of ETCs could explain the change in eddy AHT seen in Fig. 5.

ETC statistics can be considered from either an Eulerian perspective, in which frequency filtering is used to isolate synoptic-scale variability on roughly 2–6-day time scales, or from a Lagrangian one, in which an algorithm is used to identify

each individual ETC within a simulation, from which population statistics may then be calculated. As discussed by Walker et al. (2020), the Eulerian method allows for rapid calculation of ETC statistics, but without any information about the number and/or intensity of storms. For this study, we take a Lagrangian approach and consider the bulk effect of aerosol forcing on individual ETCs.

To accomplish this, we utilize the DetectNodes and StitchNodes algorithms contained within the TempestExtremesv2.1 collection (Ullrich et al. 2021) to track ETCs in the 6-hourly sea level pressure field in the CESM2-LE simulations. These individual tracks were then mapped onto a $5^\circ \times 5^\circ$ grid by counting the number of trajectories that passed through a particular grid cell during a given month. This process was applied to each of the 100 CESM2-LE simulations (although only the 50 members with smoothed BMB forcing were analyzed) and to each of the 75 CESM2-SF simulations. A full description of the method is included in the online supplemental material.

This method allows us to investigate the impact of aerosols on both the number and the intensity of ETCs. The left-hand column of Fig. 7 shows the ensemble mean climatology of the number of storms per year which pass through a given grid cell: this demonstrates that this method correctly identifies the canonical (e.g., Hoskins and Valdes 1990) Atlantic and Pacific storm tracks. Each row in the column excludes all storms

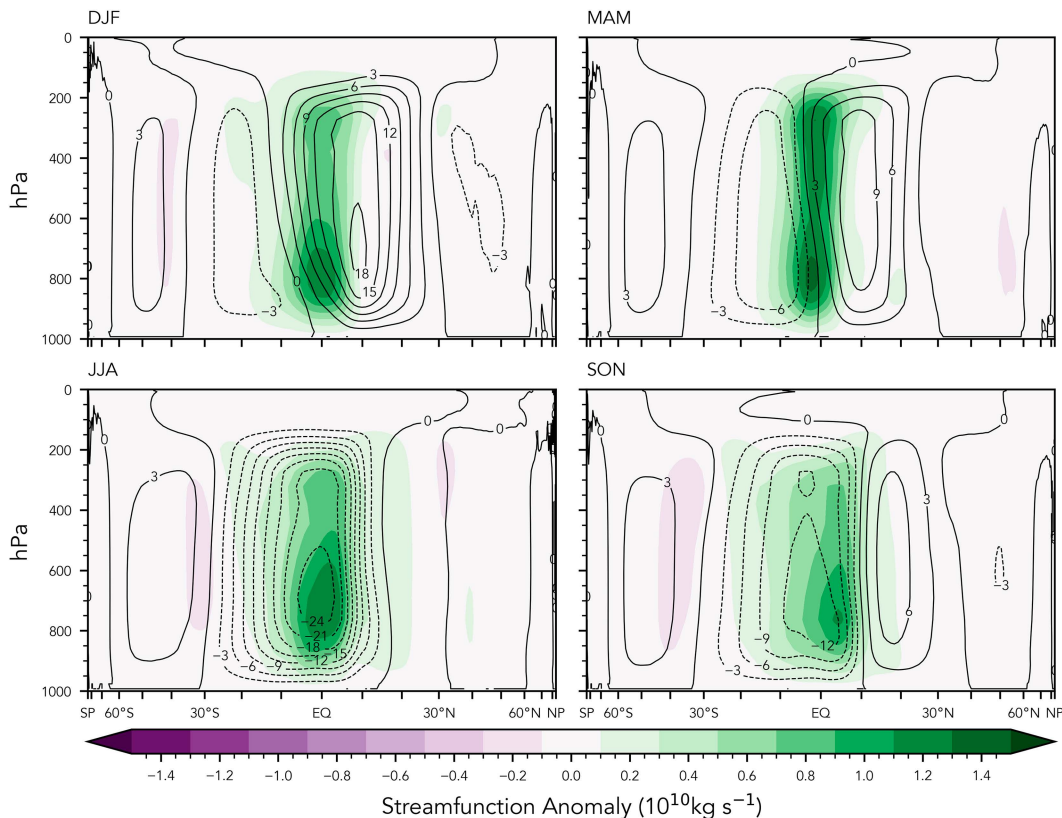


FIG. 5. Ensemble mean streamfunction anomaly by season (shading) overlaid against ensemble mean streamfunction climatology (contours, $10^{10} \text{ kg s}^{-1}$).

above a particular sea level pressure threshold so that Fig. 7a includes only the most intense storms (in which the minimum pressure along a trajectory is less than 975 hPa), while Fig. 7f includes virtually all storms identified by the algorithm. In practice, we are more concerned with the anomaly in the count of trajectories during the crucial 1960–89 period, which is shown in the right-hand column. Here, the largest change is immediately seen off of the southern tip of Greenland, where there is a marked increase in the number of the most intense storms. This is accompanied by a decrease in weaker storms over continental North America (Fig. 7f). Taken together, these changes indicate a strengthening of the Atlantic storm track that is accompanied by a poleward (and eastward) shift. There also appears to be a somewhat smaller change in the Pacific storm track.

As in Fig. 1, we can utilize the ETC track density from the various CESM2-SF subensembles to attribute the anomaly from Fig. 7 to the aerosol forcing. Figure 8 shows the smoothed time series in the number of ETCs that pass through the North Atlantic (here defined as $60^{\circ}\text{--}20^{\circ}\text{W}$, $45^{\circ}\text{--}70^{\circ}\text{N}$). The CESM2-LE anomaly shows the characteristic peak centered around 1975 that is indicative of the aerosol forcing (and is extensively discussed by NR23). In contrast, both the BMB2 and GHG2 ensembles show a negative deviation from climatology during this time period.

6. Decomposition of oceanic heat transport

As discussed previously, the OHT anomaly in the bottom-left panel of Fig. 3 is decomposed into contributions from the Atlantic and the Indo-Pacific. The Atlantic anomaly is larger than the Indo-Pacific anomaly at all latitudes and is nonnegligible from 35°S to 60°N . However, the Indo-Pacific OHT anomaly is still large from about 10°S – 30°N .

This particular decomposition (i.e., into Atlantic and Indo-Pacific contributions) is by necessity: the model output includes the northward heat transport by the global oceans and the northward heat transport in the Atlantic basin, with no separate fields for heat transport in the Pacific or Indian Ocean basins. This is partly a consequence of geography, as the boundary between the Pacific and Indian Oceans is much more porous than the boundary between either of these ocean basins and the Atlantic: consequently, there is significant heat transport between the basins, especially through the Maritime Continent (Cheng et al. 2019; Trenberth and Zhang 2019).

The canonical understanding of OHT is that it is primarily accomplished by the western boundary currents (e.g., the Gulf Stream or the Kuroshio). This can be seen in the top panel of Fig. 9 which shows the vertically integrated northward ocean heat transport calculated directly from the CESM2 ocean model output for the period from 1850 to 1899. It should be noted that Fig. 9 shows OHT data after it has

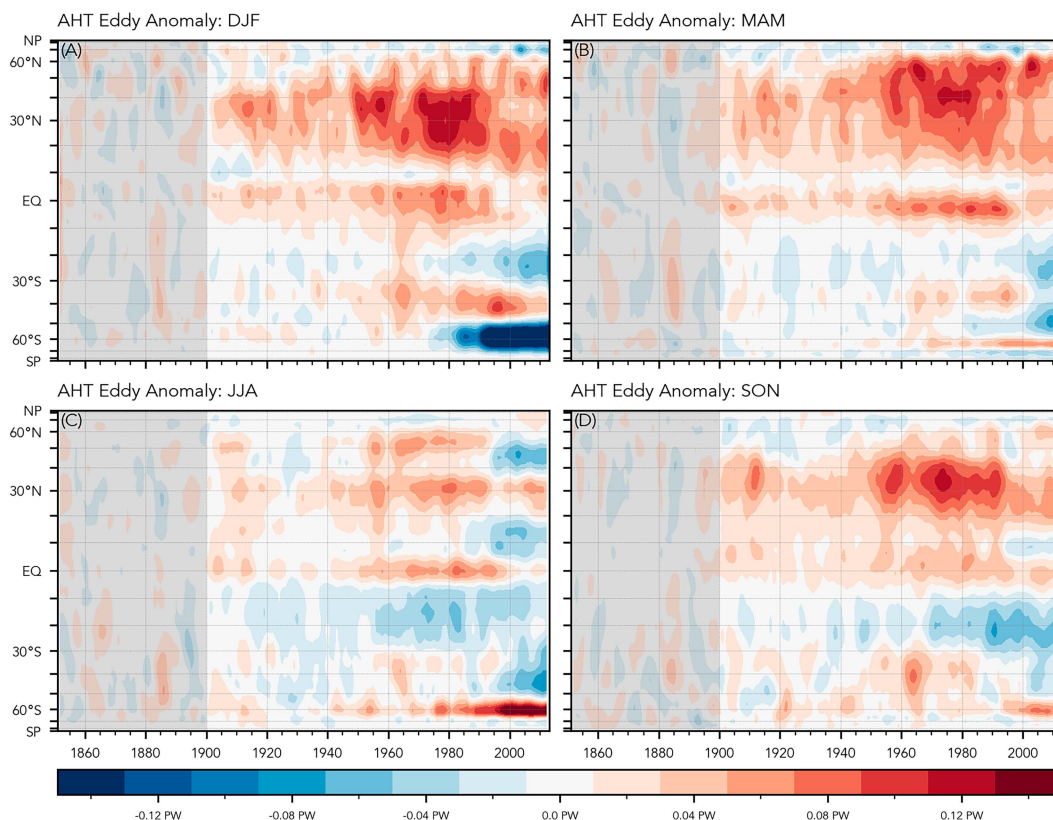


FIG. 6. As in Fig. 4, but for the combination of stationary and transient eddies.

been vertically integrated and then linearly interpolated from the irregular CESM ocean grid to a regular latitude–longitude grid for visualization purposes. The errors that accompany this interpolation are nonnegligible, so a longitudinal integration of this field (not shown) will slightly deviate from the values shown in Fig. 3. Therefore, we use this figure as a tool to identify broad regions that are important for changes in OHT but do not ascribe high confidence to the particular numerical value at any given point.

With these caveats addressed, the top panel of Fig. 9 illustrates that a large amount of energy transport is accomplished along the western boundaries of the major ocean basins—either northward (red colors) or southward (blue colors)—connected to the well-known western boundary currents. The bottom panel shows the anomaly in this ocean transport for 1960–89 relative to the above baseline. Here, the colors are largest along the east coast of the Americas, in the North Atlantic, and near the Maritime Continent, with slightly smaller values in the interior of the ocean basins, especially the Pacific. The red and blue horizontal dashed lines are included for each basin to show which regions have a nonnegligible OHT anomaly in the original heat transport from the CESM2 ocean model, as identified in Fig. 3.

a. OHT in the Atlantic

We begin our discussion of the OHT anomaly in the Atlantic basin. From Fig. 9, it is clear that the Atlantic OHT anomaly

occurs in a narrow band off the east coast of the Americas, from Brazil to New England. The cross-equatorial nature of this heat transport anomaly immediately suggests a link with the AMOC (Rahmstorf 2002; Rahmstorf et al. 2015; Thornalley et al. 2018; Caesar et al. 2018, 2021), which modeling studies have shown is particularly sensitive to anthropogenic aerosol forcing (Ma et al. 2020; Menary et al. 2020; Hassan et al. 2021; Robson et al. 2022; Li et al. 2023; Simpson et al. 2023; Needham et al. 2024).

We probe this link with Fig. 10, which shows the time series of the OHT anomaly in different seasons in the Atlantic basin. The bottom-left panel shows the seasonal- and annual-mean anomaly in the AMOC, defined as the maximum of the overturning streamfunction in the Atlantic basin below a depth of 500 m. The seasonal cycle of the AMOC anomaly is primarily due to changes in magnitude, which is consistent with the Atlantic OHT. Indeed, the Atlantic OHT at a variety of latitudes shows a remarkable similarity to the time evolution of the AMOC anomaly (right panel of Fig. 10). Correlations between the AMOC anomaly and the Atlantic OHT are extremely high, with the square of the Pearson correlation greater than 0.94 at the four latitudes shown in the panel. The interpretation here is simple: an increase in the AMOC in response to aerosol forcing is accompanied by a corresponding increase in the Atlantic OHT.

Analysis of the older CESM1 large ensemble (Kay et al. 2015) indicates that the older CESM1 ensemble does not

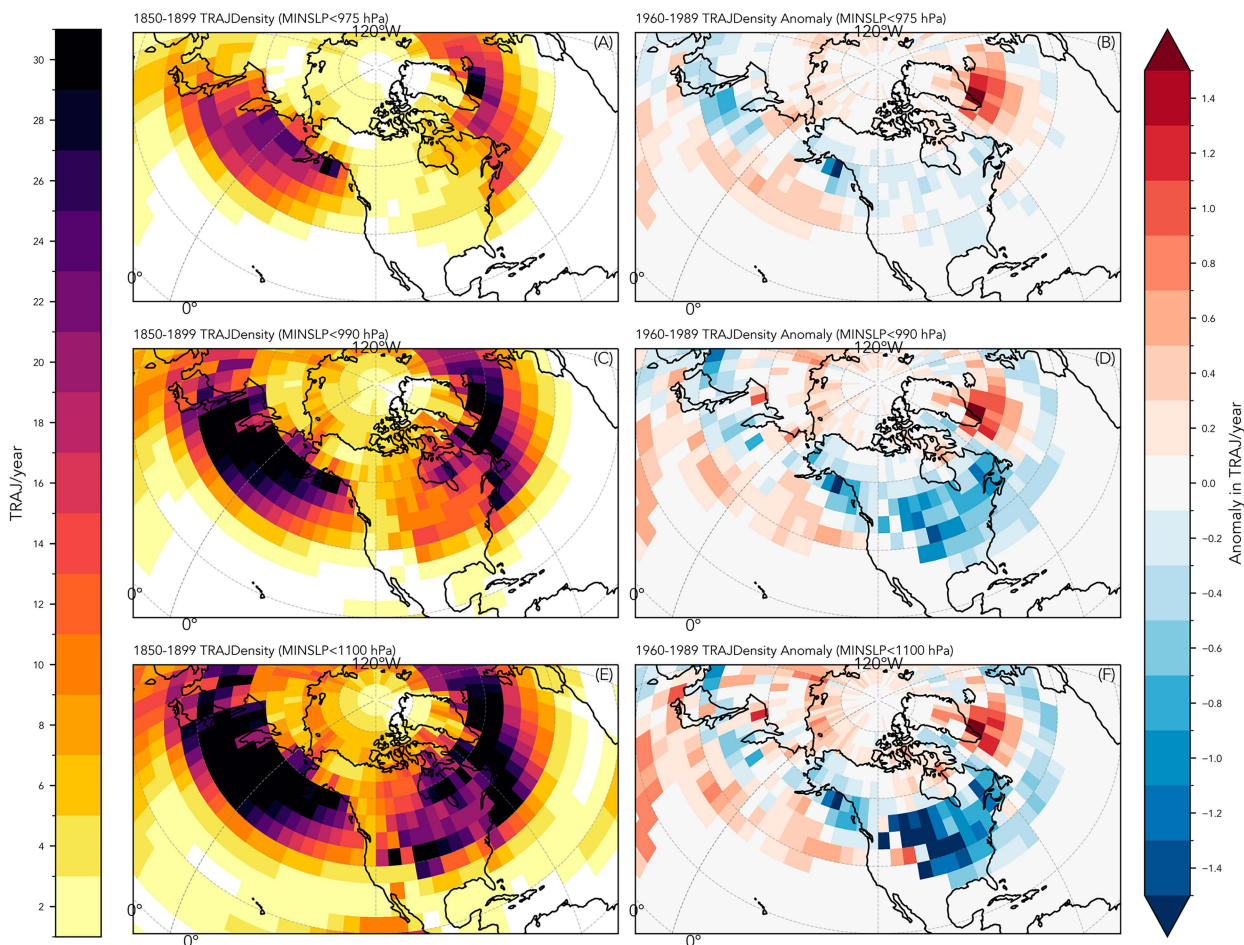


FIG. 7. (left) Ensemble mean climatology (1850–99) of the count of trajectories per year passing through a 5° grid cell. (a) Only the most intense storms (defined as the trajectories in which the minimum sea level pressure was below 975 hPa). (c) Additional strong storms (with a minimum sea level pressure below 990 hPa). (e) All identified ETCs. (right) As in the left panels, but for the anomaly in the count of ETCs from 1960 to 1989, relative to the 1850–99 climatology.

have a large anomaly in the AMOC in response to historic forcing like that seen in CESM2 (see Fig. 9 of [Simpson et al. 2023](#)). The older version also lacks the same large anomaly in the ocean heat transport, further supporting the conclusion that the large OHT anomaly in CESM2 is due to changes in the AMOC. This is consistent with recent studies ([Menary et al. 2020](#); [Hassan et al. 2021](#); [Robson et al. 2022](#); [Needham et al. 2024](#)), which found that many CMIP6 generation models (including CESM2) have a much larger AMOC response than many CMIP5 models (including CESM1) and that the AMOC response in those CMIP6 models is likely inconsistent with observations.

b. OHT in the Indo-Pacific

The remainder of this section is devoted to addressing the OHT anomaly in the broadly defined Indo-Pacific region. In contrast to the OHT anomaly in the Atlantic, which we singularly ascribe to changes in the AMOC, we find that the OHT anomaly in the Indo-Pacific is due to changes in several regions due to two distinct mechanisms.

As discussed previously, the top panel of [Fig. 9](#) indicates that the primary OHT occurs along the western boundary of the ocean basins. However, the anomaly in the OHT from 1960 to 1989 (bottom panel of [Fig. 9](#)) occurs both along the western boundaries and in the interior of the ocean basins, with the largest of these “interior anomalies” occurring in the equatorial Pacific. This is a surprising result, as the shading in the top panel would suggest that changes in the ocean interior would likely be small compared to changes along the western boundaries. However, small changes spread over a wide area can lead to large changes in the zonal integral of the heat transport (i.e., [Fig. 3](#)), which is the quantity of interest in this study. Accordingly, we now look at the factors that could have altered the heat transport in the interior of the Pacific.

1) OHT IN THE PACIFIC INTERIOR AND LINKS TO ENSO

The OHT anomaly in the central and eastern Pacific (i.e., the bottom panel of [Fig. 9](#)) is located across a wide range of longitudes but is within a narrow band of latitudes that are

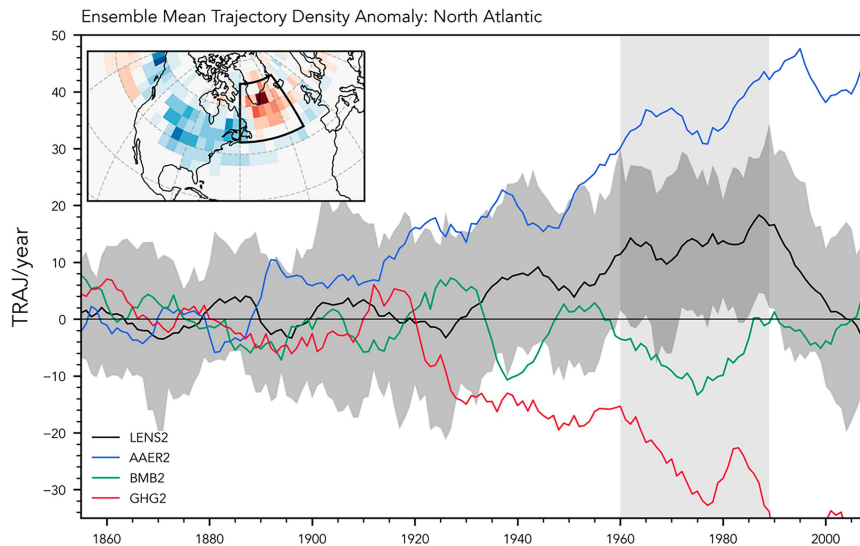


FIG. 8. Time series of the ensemble mean number of storms passing through the North Atlantic (60° – 20° W, 45° – 70° N; see the inset). The black curve shows the LENS2 anomaly (along with the interquartile range in the shading), while the blue, green, and red curves indicate the AAER2, BMB2, and GHG2 subensembles of CESM2-SF, respectively.

close to the equator. This spatial structure leads us to the hypothesis that this anomaly is in some way related to the ENSO (Trenberth 1997). We investigate this guess in the top panel of Fig. 11, which shows the anomalous OHT in the Indo-Pacific region during different phases of ENSO. The ENSO phase was determined using the 5-month average SST anomaly in the Niño-3.4 box [5° S– 5° N, 120° – 170° W, shown as the red box in the top panel of Fig. 9, equivalent to the observational oceanic Niño index (ONI)] relative to the period of 1921–70.

During El Niño months (SST anomaly ≥ 0.5 K), the OHT is anomalously positive in the Indo-Pacific, reaching an ensemble mean value of greater than half a petawatt between 5° and 10° N. During La Niña months (SST anomaly ≤ -0.5 K), the OHT anomaly is nearly the perfect inverse of the El Niño anomaly, with large negative values in excess of -0.5 PW, and during neutral months (-0.5 K \leq SST anomaly ≤ 0.5), the OHT anomaly is much smaller. This relationship between the Indo-Pacific OHT anomaly and ENSO phase occurs both in the ensemble mean of the CESM2 large ensemble (solid lines) and in a 2000-yr-long preindustrial control simulation (dashed lines) performed with CESM2 (Danabasoglu et al. 2020), which indicates that the relationship between OHT and ENSO holds in the absence of changes to external forcings.

Importantly, the magnitude of the OHT anomaly during El Niño and La Niña months is much larger than the 1960–89 anomaly in the OHT (bottom-left panel of Fig. 3 and dotted black line in the top panel of Fig. 11). As a primary characteristic of ENSO is a shift in the heat content of the eastern Pacific, this analysis suggests that a relatively small increase in the time-averaged depth of the eastern Pacific mixed layer (whether through an increase in El Niño-like conditions or

through a long-term warming trend due to GHGs) could lead to a large enough increase in the OHT to explain the anomaly seen in Fig. 3. Put another way, the increase in the depth of the time-averaged mixed layer could be much smaller than is seen during a typical El Niño event and still account for the anomaly in the OHT.

The middle panel of Fig. 11 shows two metrics that quantify the long-term behavior of the eastern Pacific, both of which show that the ensemble mean becomes more “Niño like” over the course of the historical simulations. The first measure is the ensemble mean number of El Niño minus La Niña months per year. This was calculated by first calculating the ONI time series to define Niño and Niña months for each simulation. For a particular year in a given simulation, the number of months that qualified as La Niña was subtracted from the number of months that qualified as El Niño, and then, this count was averaged across ensemble members for a given year. In the first decades of the historical period, there tend to be more La Niña than El Niño months, but over the course of the historical period, there is a general trend toward a regime that favors El Niño, especially by the end of the simulation, with a “crossover” point near the middle of the twentieth century.

The second measure is the anomaly of the depth of the mixed layer in the far eastern equatorial Pacific (averaged over the region bounded by 100° W, 85° W, 10° S, and 10° N, shown as the green box in the top panel of Fig. 9). The mixed layer becomes deeper by about a meter from 1850 to 2014 which is also consistent with a Niño-like regime as a deeper mixed layer indicates a larger heat content in the eastern tropical Pacific. For the analysis that follows, we will use the mixed-layer depth anomaly as our measure of the underlying ENSO regime because it has less high-frequency variability

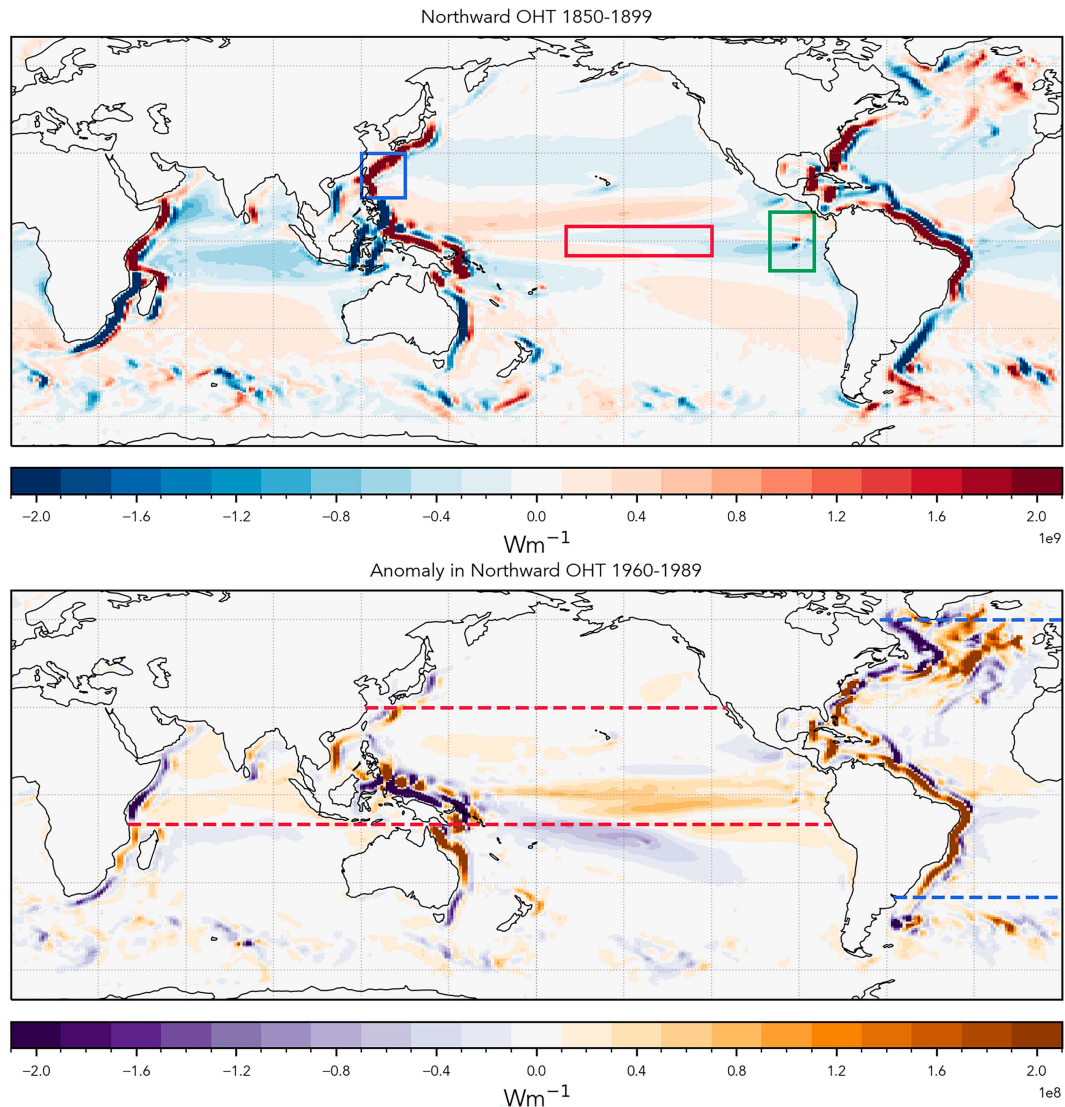


FIG. 9. Vertical integral of northward energy transport, directly calculated from the CESM2 ocean model. (top) Climatological baseline of OHT from 1850 to 1899. (bottom) Anomaly from climatology for 1960–89. Red, blue, and green boxes in the top panel are included to illustrate the Niño-3.4, Kuroshio, and eastern tropical Pacific regions that will be analyzed later in the text.

than the Niño minus Niña metric, which appears to be more sensitive to short-term forcing from things like volcanoes (e.g., the large negative spike which immediately follows the large eruption of Krakatau in 1883). The trend toward a more Niño-like regime can explain part of the increase in Indo-Pacific OHT over the historical simulations, but crucially, it cannot explain the precipitous decline in the OHT anomaly near the end of the twentieth century (shown in Fig. 3 and in the black curves of Fig. 12). This suggests that the OHT anomaly in the Indo-Pacific is also driven by some process in addition to ENSO.

To investigate this further, we return to the top panel of Fig. 9 and again note that a large fraction of the OHT occurs in the western boundary currents and make a second

educated guess that changes in the Pacific western boundary current may be important in determining the OHT anomaly. In the Indo-Pacific, the heat transport poleward of about 15°N is primarily in the westward flank of the Pacific subtropical gyre: that is, in what becomes the Kuroshio.

2) OHT IN THE PACIFIC DRIVEN BY ENSO AND KUROSHIO VARIABILITY

The bottom panel of Fig. 11 shows the ensemble mean anomaly in the strength of the Kuroshio. This was calculated as the average of the vertically integrated meridional ocean velocity in the region bounded by 120°E , 135°E , 15°N , and 30°N , shown as the blue box in the top panel of Fig. 9. The

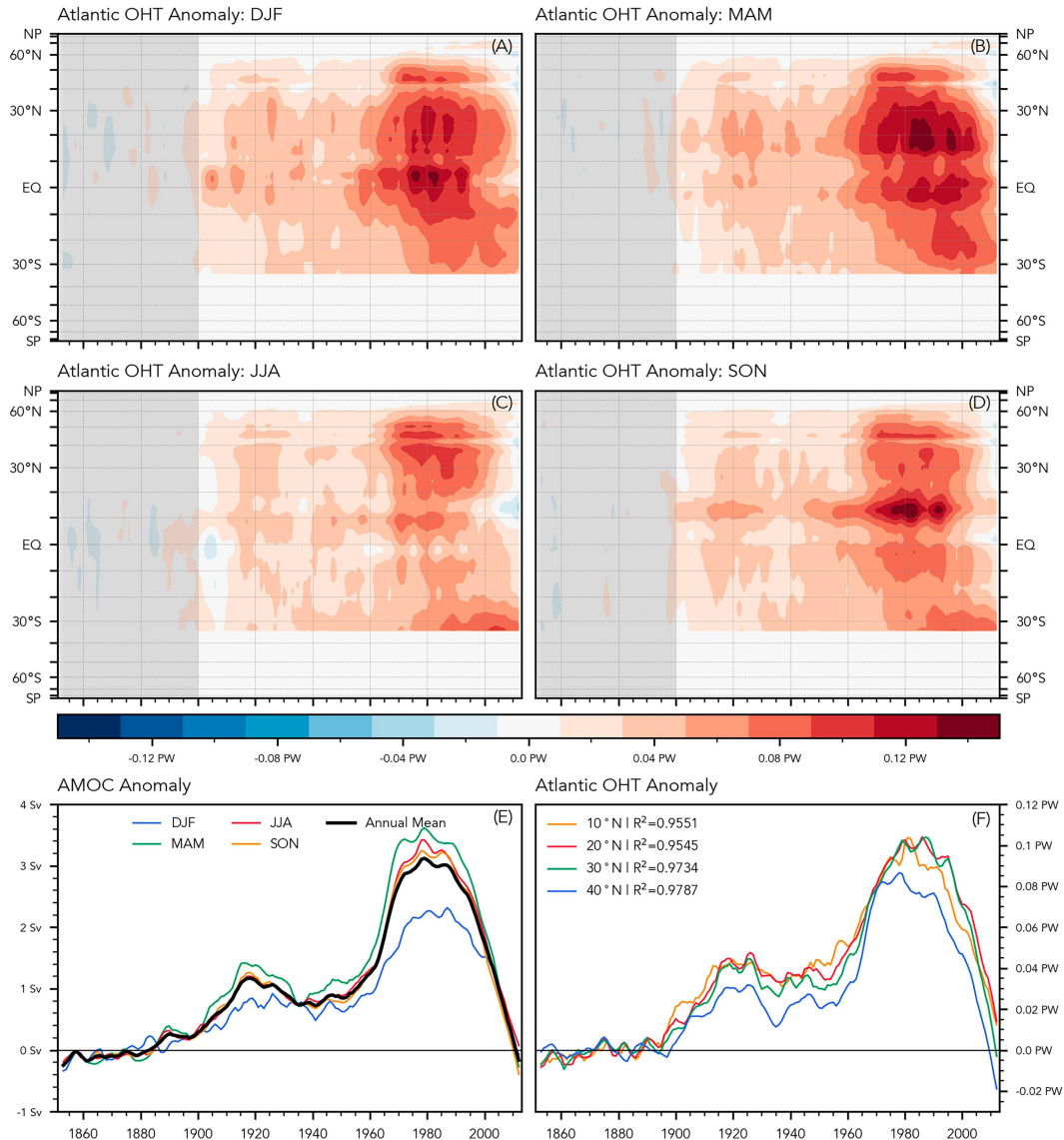


FIG. 10. (a)–(d) As in Fig. 4, but for the heat transport anomaly in the Atlantic. (e) Ensemble mean anomaly in the AMOC, defined as the maximum of the overturning streamfunction in the Atlantic basin below a depth of 500 m. (f) Ensemble mean anomaly in Atlantic OHT at a range of latitudes. Correlations in the legend are between the given OHT anomaly and the AMOC anomaly.

ensemble mean Kuroshio strength shows sensitivity to the large aerosol pulses, first in the early 1900s and then in the latter half of the twentieth century (Hoesly et al. 2018). Crucially, the anomaly becomes strongly negative in the final decade of the twentieth century and into the twenty-first century, which likely accounts for the reduction in the OHT anomaly in the Indo-Pacific.

As a test of our hypothesis that the underlying ENSO regime and the strength of the Kuroshio together explain the Indo-Pacific OHT, we perform a multiple linear regression of the form

$$Y_{\text{OHT}} = \beta_{\text{MXL}} X_{\text{MXL}} + \beta_{\text{KUR}} X_{\text{KUR}} + \alpha, \quad (1)$$

where the “prediction” Y_{OHT} is the area-weighted average OHT anomaly in the Indo-Pacific between 10°S and 30°N, the first predictor X_{MXL} is the anomaly in the depth of the mixed layer in the extreme eastern tropical Pacific (i.e., the green curve in the middle panel of Fig. 11), the second predictor X_{KUR} is the anomaly in the strength of the Kuroshio (i.e., the blue curve in the bottom panel of Fig. 11), β_{MXL} and β_{KUR} are the regression coefficients (i.e., slope), and α is the intercept.

In contrast to earlier analysis, this multiple linear regression was performed using all 100 ensemble members. When only the 50 members with smoothed BMB forcing were used, a 40/10 split of ensemble members into training and testing groups

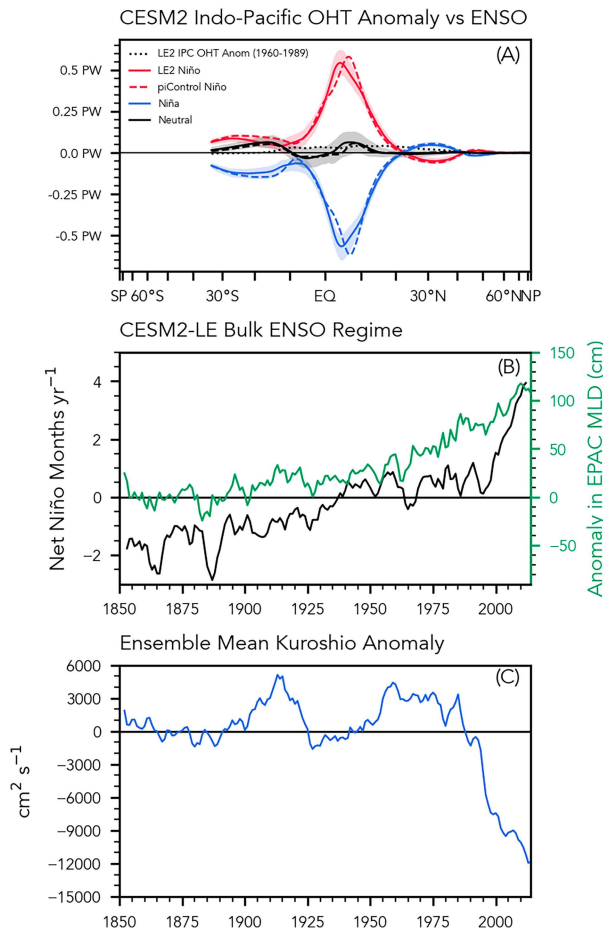


FIG. 11. (a) Composite analysis showing the anomalous OHT in the Indo-Pacific region during different phases of ENSO for the CESM2-LE (solid lines) and for the CESM2 preindustrial control simulation (dashed lines). Shading shows the model spread, quantified as the 5th–95th percentile among ensemble members. Also shown is the heat transport anomaly in the Indo-Pacific from 1960 to 1989, which is identical to the corresponding curve in the bottom-left panel of Fig. 3. (b) Time series of two metrics used to quantify changes in the ensemble mean ENSO regime in the CESM2 large ensemble. The black curve shows the ensemble average number of El Niño minus La Niña months for each year, while the green curve shows the anomaly in the depth of the mixed layer (positive indicating a deeper mixed layer) in the eastern tropical Pacific. (c) Time series of the ensemble mean anomaly of the strength of the Kuroshio (defined as the average vertically integrated ocean velocity from 120° to 135°E and 15° to 30°N).

led to too much noise in the ensemble mean of only 10 members. We performed this analysis using only the 50 members with smoothed BMB forcing as well as with only the 50 members with the original CMIP6 forcing and found no discernible difference between the sets. This allows us to be confident that the results of the multiple linear regression are not due to a difference in the response to BMB forcing but simply require a sample size larger than 50 members to isolate the forced response from internal variability.

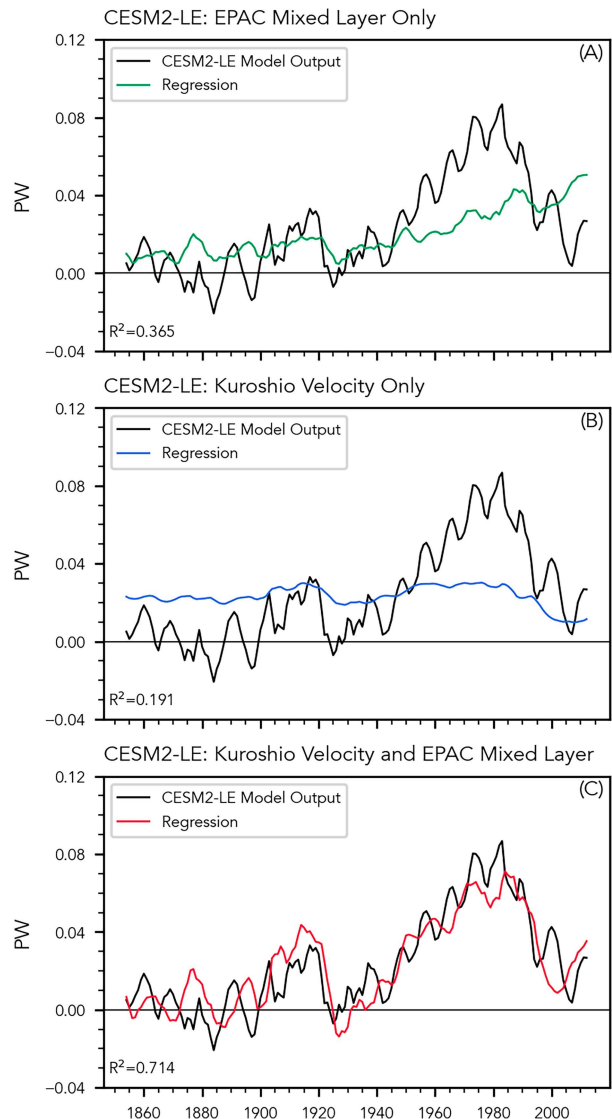


FIG. 12. Comparison of the average heat transport anomaly from 10°S to 30°N in the Indo-Pacific (black curve) and the value predicted by a linear regression against (a) the mixed-layer depth anomaly in the eastern Pacific, (b) the Kuroshio strength anomaly, and (c) against both the mixed-layer depth and the Kuroshio anomalies.

To prevent overfitting, which is an important consideration even for a linear model, we randomly divided our 100 ensemble members into two groups, with 80 members (the training set) used to generate regression coefficients and the final 20 members (the testing set) used for evaluation of the model fit. Given our training and testing sets, we then took a bootstrapping approach where 5000 random subsets of 20 training set ensemble members were used to generate a set of regression coefficients and an intercept. Finally, the average regression coefficients and intercept were used with the testing set to “predict” the ocean heat transport anomaly from the anomalies in the eastern Pacific mixed-layer depth and the Kuroshio strength.

This prediction using the testing set mixed-layer depth and Kuroshio strength is shown as the red curve in the bottom panel of Fig. 12 against the testing set ensemble mean OHT anomaly. The linear model largely recreates the low-frequency behavior of the OHT anomaly ($R^2 = 0.714$) with a first peak in the early 1900s and a second, larger peak that reaches its maximum deviation from climatology in the 1980s. When this process was repeated using only the mixed-layer depth or only the Kuroshio strength as predictors, the prediction failed to adequately recreate the OHT anomaly (top and middle panels of Fig. 12; R^2 of 0.365 and 0.191, respectively). This emphasizes that both the underlying ENSO state and the variability of the Kuroshio are necessary to explain the heat transport anomaly simulated by the large ensemble.

7. Discussion

We have taken a distributed approach in this study and systematically worked through the various components that contribute to the PET separately. This was useful for gaining a better understanding of the processes that drive the different contributors to PET, but ignores the fact that none of these processes truly act in isolation. Therefore, we briefly discuss some of the interactions between these processes.

a. Thermally direct Hadley cells and wind-driven Kuroshio

The change in the ENSO regime toward more Niño-like months can be easily understood as a direct consequence of the warming associated with increasing greenhouse gas forcing. The change in the Kuroshio requires a longer—but still brief—explanation.

The Kuroshio is one of the western boundary currents required to balance the equatorward mass transport in the Pacific interior, as predicted by Sverdrup theory (e.g., Hartmann 2016). This mass transport is driven by the latitudinal shear of the horizontal wind, with westward surface winds near the equator and eastward surface winds in the midlatitudes across the span of the Pacific. The strength of the equatorial winds (i.e., the trades) is driven in turn by the lower branch of the Hadley cell, which curves from primarily meridional to primarily zonal due to the influence of the Coriolis effect.

We have shown previously (Fig. 5) that an anomalous Hadley circulation develops centered over the equator in response to Northern Hemisphere aerosol forcing. Through angular momentum conservation, the stronger meridional surface flow associated with this anomalous Hadley cell implies an increase in the magnitude of the zonal trade winds over the equatorial Pacific. This increase in the latitudinal wind shear then implies an increase in the southward mass transport in the Pacific interior and, by extension, an increase in the northward mass transport by the western boundary current.

Taken together, our results suggest that aerosol forcing in the northern midlatitudes led to an anomalous Hadley cell centered over the equator, which increased the magnitude of the trade winds over the Pacific. These stronger trades increased the wind stress on the Pacific subtropical gyre which implies (by Sverdrup theory) a strengthening of the western

boundary current and a corresponding increase in northward oceanic heat transport in the Pacific.

b. Ocean currents and extratropical cyclones

The increase in the frequency of ETCs (Fig. 7) is primarily located off the southern tip of Greenland (with a somewhat smaller change in the Pacific). This indicates a straightforward relationship between changes in the AMOC (Fig. 10) and the changes in the frequency of intense ETCs. The logic here is essentially the inverse of the so-called North Atlantic warming hole (Chemke et al. 2020; Keil et al. 2020, e.g.) in which a decrease in the strength of the AMOC is associated with an isolated region of decadal-scale cooling. In these simulations, the AMOC increase in response to aerosol forcing suggests a region of enhanced SSTs, which would support the formation and growth of ETCs.

A recent study by Needham et al. (2024) demonstrated that the large AMOC anomaly observed in the CESM2-LE compared to the earlier CESM1 large ensemble (CESM1-LE Kay et al. 2015) was largely explained by a change in the temporal variability of turbulent heat fluxes in the North Atlantic. They further proposed the hypothesis that this variability may result from an increase in the temporal variability of CMIP6 generation forcings (including aerosols) compared to the older CMIP5 generation forcings. Additionally, they showed that the AMOC response to aerosols lags the response of the surface heat fluxes by 2–4 years.

In the context of this work, the results of that study suggest a positive feedback loop where increased cyclonic activity increases the turbulent heat fluxes from the ocean to the atmosphere, which in turn increases the strength of the AMOC, leading to warmer waters that support the growth of additional extratropical cyclones. It is possible that the increase in the frequency of intense extratropical cyclones shown in this study may explain the enhanced surface heat flux variability described by Needham et al. (2024). If so, this would suggest that ETC changes are in some way linked to the increased interannual variability of the CMIP6 aerosol forcing. Another possibility (which is not mutually exclusive) is that this mechanism is somehow related to changes in the North Atlantic Oscillation (Hurrell et al. 2003) which is known to play an important role in the characteristics of Atlantic storms, but this has not been explored.

c. Conclusions

The goal of this study was to continue the work of Needham and Randall (2023) and identify which physical processes led to the positive anomaly in the integrated poleward energy transport, which that study attributed to a change in anthropogenic aerosol forcing. From this study, it should be clear that heat transport by the atmosphere and oceans is accomplished by a collection of interdependent physical processes, which combine to yield a PET which is a smooth, almost sinusoidal function of latitude constrained only by the top of the atmosphere radiative balance (Stone 1978; Trenberth and Stepaniak 2003). To analyze this complex web of interactions and to understand how they respond to historical forcings, we found it useful to systematically

work through these various components. This led us to separate the heat transport anomaly into atmospheric heat transport by the MMC and transient eddies (i.e., extratropical cyclones) and oceanic transport in the Atlantic and Indo-Pacific basins. The decomposition into these various anomalies provided clues about which aspects of the climate system were responsible for the change in the total poleward energy transport.

In the atmosphere, we found that both the MMC and transient eddies changed to accomplish the required heat transport. Strong extratropical cyclones became more common in the North Atlantic, and an anomalous Hadley circulation developed on the equator which shifted the ITCZ southward while at the same time exporting additional energy northward.

In the oceans, the more complicated contribution occurred in the broadly defined Indo-Pacific basin. Here, we found that the heat transport anomaly occurred both in the interior of the Pacific (primarily due to a change in the ENSO regime) and along the western boundary (attributed to changes in the Kuroshio/the wind-driven ocean gyre). In the Atlantic, we ascribed changes in the OHT anomaly to a strengthening of the Atlantic meridional overturning circulation.

Previous studies have shown that the AMOC response is overly sensitive to aerosol forcing in many members of the CMIP6 class of models (Menary et al. 2020; Hassan et al. 2021; Robson et al. 2022), which likely includes CESM2 (Simpson et al. 2023). This suggests that CESM2 likely overestimates the Atlantic heat transport anomaly and by extension the total oceanic plus atmospheric heat transport anomaly, as well as the increase in ETC activity.

We do not believe that this overactive AMOC would indicate that the total PET anomaly (i.e., the OHT plus AHT) described here and in NR23 is entirely fictitious; indeed, comparison of the CESM2 large ensemble with the earlier CESM1 large ensemble (Kay et al. 2015) shows that both versions of CESM produce a heat transport anomaly in response to historic aerosol forcing although the heat transport and AMOC responses are smaller in CESM1. Additionally, NR23 found that the ERA5 atmospheric reanalysis showed a decrease in the total PET from the 1980s to the near present. Finally, observational studies have shown a historic southward shift of the tropical rainband which has been attributed to anomalous cross-equatorial heat transport by the atmospheric MMC in response to anthropogenic aerosol forcing (Hwang et al. 2013; Allen et al. 2015; Irving et al. 2019; Lembo et al. 2019; Yukimoto et al. 2022).

However, we do conclude that the large AMOC response and corresponding large OHT anomaly in the Atlantic—alongside the related atmospheric eddy heat transport in the Atlantic storm track—indicate that the historic PET anomaly predicted by the ensemble mean of the CESM2 large ensemble is likely too large although it is difficult to quantify the magnitude of this overprediction. Satellite measurement of Earth's energy balance is the only direct way to accurately measure this total transport, and continuous observations only exist for the twenty-first century (Loeb et al. 2018). In the absence of a continuous observational record covering the twentieth century, we must instead rely on observations and reconstructions of various phenomena (e.g., historical observations

of the AMOC change Rahmstorf et al. 2015; Caesar et al. 2018; Menary et al. 2020; Caesar et al. 2021) to constrain the past changes in poleward energy transport.

Acknowledgments. This work was supported by the National Oceanic and Atmospheric Administration through Grant NA19OAR4590155 and the National Science Foundation through Grant AGS-1826643, both to the Colorado State University.

Data availability statement. Model output from the CESM2-LE is available at <https://www.cesm.ucar.edu/community-projects/lens2>. Output from the CESM2 preindustrial control simulation is available from the Earth System Grid Federation at https://esgf-node.llnl.gov/search/cmip6/?institution_id=NCAR&source_id=CESM2&experiment_id=piControl&variant_label=r1i1p1f1. Data analysis was performed in Python alongside data postprocessing and subsetting performed using netCDF operators (<https://nco.sourceforge.net/nco.pdf>). Multiple linear regressions were performed using scikit-learn (<https://scikit-learn.org/stable/>). Output files from tracking extratropical cyclones with Tempest-Extremes are available online and can be found using the following doi: <https://doi.org/10.5281/zenodo.11406533>.

REFERENCES

- Adam, O., T. Bischoff, and T. Schneider, 2016: Seasonal and interannual variations of the energy flux equator and ITCZ. Part I: Zonally averaged ITCZ position. *J. Climate*, **29**, 3219–3230, <https://doi.org/10.1175/JCLI-D-15-0512.1>.
- Allen, R. J., A. T. Evan, and B. B. Booth, 2015: Interhemispheric aerosol radiative forcing and tropical precipitation shifts during the late twentieth century. *J. Climate*, **28**, 8219–8246, <https://doi.org/10.1175/JCLI-D-15-0148.1>.
- Armour, K. C., N. Siler, A. Donohoe, and G. H. Roe, 2019: Meridional atmospheric heat transport constrained by energetics and mediated by large-scale diffusion. *J. Climate*, **32**, 3655–3680, <https://doi.org/10.1175/JCLI-D-18-0563.1>.
- Bjerknes, J., 1964: Atlantic air-sea interaction. *Advances in Geophysics*, Vol. 10, H.E. Landsberg and J. Van Mieghem, Eds., Academic Press, 1–82, [https://doi.org/10.1016/S0065-2687\(08\)60005-9](https://doi.org/10.1016/S0065-2687(08)60005-9).
- Caesar, L., S. Rahmstorf, A. Robinson, G. Feulner, and V. Saba, 2018: Observed fingerprint of a weakening Atlantic Ocean overturning circulation. *Nature*, **556**, 191–196, <https://doi.org/10.1038/s41586-018-0006-5>.
- , G. D. McCarthy, D. J. R. Thornalley, N. Cahill, and S. Rahmstorf, 2021: Current Atlantic meridional overturning circulation weakest in last millennium. *Nat. Geosci.*, **14**, 118–120, <https://doi.org/10.1038/s41561-021-00699-z>.
- Chemke, R., L. Zanna, and L. M. Polvani, 2020: Identifying a human signal in the North Atlantic warming hole. *Nat. Commun.*, **11**, 1540, <https://doi.org/10.1038/s41467-020-15285-x>.
- Cheng, L., K. E. Trenberth, J. T. Fasullo, M. Mayer, M. Balmaseda, and J. Zhu, 2019: Evolution of ocean heat content related to ENSO. *J. Climate*, **32**, 3529–3556, <https://doi.org/10.1175/JCLI-D-18-0607.1>.
- Chiang, J. C. H., and C. M. Bitz, 2005: Influence of high latitude ice cover on the marine intertropical convergence zone.

- Climate Dyn.*, **25**, 477–496, <https://doi.org/10.1007/s00382-005-0040-5>.
- Cox, T., A. Donohoe, G. H. Roe, K. C. Armour, and D. M. W. Frierson, 2022: Near invariance of poleward atmospheric heat transport in response to midlatitude orography. *J. Climate*, **35**, 4099–4113, <https://doi.org/10.1175/JCLI-D-21-0888.1>.
- Czaja, A., and J. Marshall, 2006: The partitioning of poleward heat transport between the atmosphere and ocean. *J. Atmos. Sci.*, **63**, 1498–1511, <https://doi.org/10.1175/JAS3695.1>.
- Danabasoglu, G., and Coauthors, 2020: The Community Earth System Model version 2 (CESM2). *J. Adv. Model. Earth Syst.*, **12**, e2019MS001916, <https://doi.org/10.1029/2019MS001916>.
- Deser, C., and Coauthors, 2020: Isolating the evolving contributions of anthropogenic aerosols and greenhouse gases: A new CESM1 large ensemble community resource. *J. Climate*, **33**, 7835–7858, <https://doi.org/10.1175/JCLI-D-20-0123.1>.
- Donohoe, A., and A. Voigt, 2017: Why future shifts in tropical precipitation will likely be small: The location of the tropical rain belt and the hemispheric contrast of energy input to the atmosphere. *Climate Extremes: Patterns and Mechanisms*, *Geophys. Monogr.*, Vol. 6, Amer. Geophys. Union, 115–137, <https://doi.org/10.1002/9781119068020.ch8>.
- Enderton, D., and J. Marshall, 2009: Explorations of atmosphere–ocean–ice climates on an aquaplanet and their meridional energy transports. *J. Atmos. Sci.*, **66**, 1593–1611, <https://doi.org/10.1175/2008JAS2680.1>.
- Eyring, V., S. Bony, G. A. Meehl, C. A. Senior, B. Stevens, R. J. Stouffer, and K. E. Taylor, 2016: Overview of the Coupled Model Intercomparison Project phase 6 (CMIP6) experimental design and organization. *Geosci. Model Dev.*, **9**, 1937–1958, <https://doi.org/10.5194/gmd-9-1937-2016>.
- Fasullo, J. T., J.-F. Lamarque, C. Hannay, N. Rosenbloom, S. Tilmes, P. DeRepentigny, A. Jahn, and C. Deser, 2022: Spurious late historical-era warming in CESM2 driven by prescribed biomass burning emissions. *Geophys. Res. Lett.*, **49**, e2021GL097420, <https://doi.org/10.1029/2021GL097420>.
- Frierson, D. M. W., and Coauthors, 2013: Contribution of ocean overturning circulation to tropical rainfall peak in the Northern Hemisphere. *Nat. Geosci.*, **6**, 940–944, <https://doi.org/10.1038/ngeo1987>.
- Hartmann, D. L., 2016: *Global Physical Climatology*. Elsevier, 485 pp.
- Hassan, T., R. J. Allen, W. Liu, and C. A. Randles, 2021: Anthropogenic aerosol forcing of the Atlantic meridional overturning circulation and the associated mechanisms in CMIP6 models. *Atmos. Chem. Phys.*, **21**, 5821–5846, <https://doi.org/10.5194/acp-21-5821-2021>.
- Held, I. M., 2001: The partitioning of the poleward energy transport between the tropical ocean and atmosphere. *J. Atmos. Sci.*, **58**, 943–948, [https://doi.org/10.1175/1520-0469\(2001\)058<0943:TPOTPE>2.0.CO;2](https://doi.org/10.1175/1520-0469(2001)058<0943:TPOTPE>2.0.CO;2).
- Hersbach, H., and Coauthors, 2020: The ERA5 global reanalysis. *Quart. J. Roy. Meteor. Soc.*, **146**, 1999–2049, <https://doi.org/10.1002/qj.3803>.
- Hoelsy, R. M., and Coauthors, 2018: Historical (1750–2014) anthropogenic emissions of reactive gases and aerosols from the Community Emissions Data System (CEDS). *Geosci. Model Dev.*, **11**, 369–408, <https://doi.org/10.5194/gmd-11-369-2018>.
- Hoskins, B. J., and P. J. Valdes, 1990: On the existence of stormtracks. *J. Atmos. Sci.*, **47**, 1854–1864, [https://doi.org/10.1175/1520-0469\(1990\)047%3C1854:OTEOST%3E2.0.CO;2](https://doi.org/10.1175/1520-0469(1990)047%3C1854:OTEOST%3E2.0.CO;2).
- Hoyer, S., and J. Hamman, 2017: xarray: N-D labeled arrays and datasets in Python. *J. Open Res. Software*, **5**, 10, <https://doi.org/10.5334/jors.148>.
- Hurrell, J. W., Y. Kushnir, G. Ottersen, and M. Visbeck, 2003: An overview of the North Atlantic Oscillation. *The North Atlantic Oscillation: Climatic Significance and Environmental Impact*, *Geophys. Monogr.*, Vol. 134, Amer. Geophys. Union, 1–35, <https://doi.org/10.1029/134GM01>.
- Hwang, Y.-T., D. M. W. Frierson, and S. M. Kang, 2013: Anthropogenic sulfate aerosol and the southward shift of tropical precipitation in the late 20th century. *Geophys. Res. Lett.*, **40**, 2845–2850, <https://doi.org/10.1002/grl.50502>.
- Irving, D. B., S. Wjffels, and J. A. Church, 2019: Anthropogenic aerosols, greenhouse gases, and the uptake, transport, and storage of excess heat in the climate system. *Geophys. Res. Lett.*, **46**, 4894–4903, <https://doi.org/10.1029/2019GL082015>.
- Kang, S. M., 2020: Extratropical influence on the tropical rainfall distribution. *Curr. Climate Change Rep.*, **6**, 24–36, <https://doi.org/10.1007/s40641-020-00154-y>.
- , I. M. Held, D. M. W. Frierson, and M. Zhao, 2008: The response of the ITCZ to extratropical thermal forcing: Idealized slab-ocean experiments with a GCM. *J. Climate*, **21**, 3521–3532, <https://doi.org/10.1175/2007JCLI2146.1>.
- Kay, J. E., and Coauthors, 2015: The Community Earth System Model (CESM) large ensemble project: A community resource for studying climate change in the presence of internal climate variability. *Bull. Amer. Meteor. Soc.*, **96**, 1333–1349, <https://doi.org/10.1175/BAMS-D-13-00255.1>.
- Keil, P., T. Mauritsen, J. Jungclaus, C. Hedemann, D. Olonscheck, and R. Ghosh, 2020: Multiple drivers of the North Atlantic warming hole. *Nat. Climate Change*, **10**, 667–671, <https://doi.org/10.1038/s41558-020-0819-8>.
- Kiehl, J. T., and K. E. Trenberth, 1997: Earth's annual global mean energy budget. *Bull. Amer. Meteor. Soc.*, **78**, 197–208, [https://doi.org/10.1175/1520-0477\(1997\)078<0197:EAGMEB>2.0.CO;2](https://doi.org/10.1175/1520-0477(1997)078<0197:EAGMEB>2.0.CO;2).
- Knietzsch, M.-A., A. Schröder, V. Lucarini, and F. Lunkeit, 2015: The impact of oceanic heat transport on the atmospheric circulation. *Earth Syst. Dyn.*, **6**, 591–615, <https://doi.org/10.5194/esd-6-591-2015>.
- Lembo, V., D. Folini, M. Wild, and P. Lionello, 2019: Inter-hemispheric differences in energy budgets and cross-equatorial transport anomalies during the 20th century. *Climate Dyn.*, **53**, 115–135, <https://doi.org/10.1007/s00382-018-4572-x>.
- Li, S., W. Liu, R. J. Allen, J.-R. Shi, and L. Li, 2023: Ocean heat uptake and interbasin redistribution driven by anthropogenic aerosols and greenhouse gases. *Nat. Geosci.*, **16**, 695–703, <https://doi.org/10.1038/s41561-023-01219-x>.
- Loeb, N. G., and Coauthors, 2018: Clouds and the Earth's Radiant Energy System (CERES) Energy Balanced and Filled (EBAF) top-of-atmosphere (TOA) edition-4.0 data product. *J. Climate*, **31**, 895–918, <https://doi.org/10.1175/JCLI-D-17-0208.1>.
- Ma, X., W. Liu, R. J. Allen, G. Huang, and X. Li, 2020: Dependence of regional ocean heat uptake on anthropogenic warming scenarios. *Sci. Adv.*, **6**, eabc0303, <https://doi.org/10.1126/sciadv.abc0303>.
- Marshall, J., A. Donohoe, D. Ferreira, and D. McGee, 2014: The Ocean's role in setting the mean position of the Inter-Tropical Convergence Zone. *Climate Dyn.*, **42**, 1967–1979, <https://doi.org/10.1007/s00382-013-1767-z>.

- Menary, M. B., and Coauthors, 2020: Aerosol-forced AMOC changes in CMIP6 historical simulations. *Geophys. Res. Lett.*, **47**, e2020GL088166, <https://doi.org/10.1029/2020GL088166>.
- Ming, Y., and V. Ramaswamy, 2011: A model investigation of aerosol-induced changes in tropical circulation. *J. Climate*, **24**, 5125–5133, <https://doi.org/10.1175/2011JCLI4108.1>.
- Needham, M. R., and D. A. Randall, 2021: Riehl and Malkus revisited: The role of cloud radiative effects. *J. Geophys. Res. Atmos.*, **126**, e2021JD035019, <https://doi.org/10.1029/2021JD035019>.
- , and —, 2023: Anomalous northward energy transport due to anthropogenic aerosols during the twentieth century. *J. Climate*, **36**, 6713–6728, <https://doi.org/10.1175/JCLI-D-22-0798.1>.
- , D. D. Falter, and D. A. Randall, 2024: Changes in external forcings drive divergent AMOC responses across CESM generations. *Geophys. Res. Lett.*, **51**, e2023GL106410, <https://doi.org/10.1029/2023GL106410>.
- Neelin, J. D., and I. M. Held, 1987: Modeling tropical convergence based on the moist static energy budget. *Mon. Wea. Rev.*, **115**, 3–12, [https://doi.org/10.1175/1520-0493\(1987\)115<0003:MTCBOT>2.0.CO;2](https://doi.org/10.1175/1520-0493(1987)115<0003:MTCBOT>2.0.CO;2).
- Oort, A. H., 1971: The observed annual cycle in the meridional transport of atmospheric energy. *J. Atmos. Sci.*, **28**, 325–339, [https://doi.org/10.1175/1520-0469\(1971\)028<0325:TOACIT>2.0.CO;2](https://doi.org/10.1175/1520-0469(1971)028<0325:TOACIT>2.0.CO;2).
- Pearce, F. A., and A. Bodas-Salcedo, 2023: Implied heat transport from CERES data: Direct radiative effect of clouds on regional patterns and hemispheric symmetry. *J. Climate*, **36**, 4019–4030, <https://doi.org/10.1175/JCLI-D-22-0149.1>.
- Rahmstorf, S., 2002: Ocean circulation and climate during the past 120,000 years. *Nature*, **419**, 207–214, <https://doi.org/10.1038/nature01090>.
- , J. E. Box, G. Feulner, M. E. Mann, A. Robinson, S. Rutherford, and E. J. Schaffernicht, 2015: Exceptional twentieth-century slowdown in Atlantic Ocean overturning circulation. *Nat. Climate Change*, **5**, 475–480, <https://doi.org/10.1038/nclimate2554>.
- Ramanathan, V., 1987: The role of earth radiation budget studies in climate and general circulation research. *J. Geophys. Res.*, **92**, 4075–4095, <https://doi.org/10.1029/JD092iD04p04075>.
- , R. D. Cess, E. F. Harrison, P. Minnis, B. R. Barkstrom, E. Ahmad, and D. Hartmann, 1989: Cloud–radiative forcing and climate: Results from the Earth radiation budget experiment. *Science*, **243**, 57–63, <https://doi.org/10.1126/science.243.4887.57>.
- Riehl, H., and J. S. Malkus, 1958: On the heat balance in the equatorial trough zone. *Geophysica*, **6**, 503–537.
- Robson, J., and Coauthors, 2022: The role of anthropogenic aerosol forcing in the 1850–1985 strengthening of the AMOC in CMIP6 historical simulations. *J. Climate*, **35**, 6843–6863, <https://doi.org/10.1175/JCLI-D-22-0124.1>.
- Rodgers, K. B., and Coauthors, 2021: Ubiquity of human-induced changes in climate variability. *Earth Syst. Dyn.*, **12**, 1393–1411, <https://doi.org/10.5194/esd-12-1393-2021>.
- Rose, B. E. J., and D. Ferreira, 2012: Ocean heat transport and water vapor greenhouse in a warm equable climate: A new look at the low gradient paradox. *J. Climate*, **26**, 2117–2136, <https://doi.org/10.1175/JCLI-D-11-00547.1>.
- Schneider, T., T. Bischoff, and G. H. Haug, 2014: Migrations and dynamics of the intertropical convergence zone. *Nature*, **513**, 45–53, <https://doi.org/10.1038/nature13636>.
- Shaw, T. A., and Z. Smith, 2022: The midlatitude response to polar sea ice loss: Idealized Slab-Ocean aquaplanet experiments with thermodynamic sea ice. *J. Climate*, **35**, 2633–2649, <https://doi.org/10.1175/JCLI-D-21-0508.1>.
- Simpson, I. R., and Coauthors, 2023: The CESM2 single-forcing large ensemble and comparison to CESM1: Implications for experimental design. *J. Climate*, **36**, 5687–5711, <https://doi.org/10.1175/JCLI-D-22-0666.1>.
- Stone, P. H., 1978: Constraints on dynamical transports of energy on a spherical planet. *Dyn. Atmos. Oceans*, **2**, 123–139, [https://doi.org/10.1016/0377-0265\(78\)90006-4](https://doi.org/10.1016/0377-0265(78)90006-4).
- Sverdrup, H. U., M. W. Johnson, and R. H. Fleming, 1942: *The Oceans, Their Physics, Chemistry, and General Biology*. Prentice Hall, Inc., 1087 pp.
- Thornalley, D. J. R., and Coauthors, 2018: Anomalous weak Labrador Sea convection and Atlantic overturning during the past 150 years. *Nature*, **556**, 227–230, <https://doi.org/10.1038/s41586-018-0007-4>.
- Trenberth, K. E., 1979: Mean annual poleward energy transports by the oceans in the Southern Hemisphere. *Dyn. Atmos. Oceans*, **4**, 57–64, [https://doi.org/10.1016/0377-0265\(79\)90052-6](https://doi.org/10.1016/0377-0265(79)90052-6).
- , 1997: The definition of El Niño. *Bull. Amer. Meteor. Soc.*, **78**, 2771–2778, [https://doi.org/10.1175/1520-0477\(1997\)078%3C2771:TDOENO%3E2.0.CO;2](https://doi.org/10.1175/1520-0477(1997)078%3C2771:TDOENO%3E2.0.CO;2).
- , and D. P. Stepaniak, 2003: Seamless poleward atmospheric energy transports and implications for the Hadley circulation. *J. Climate*, **16**, 3706–3722, [https://doi.org/10.1175/1520-0442\(2003\)016%3C3706:SPAETA%3E2.0.CO;2](https://doi.org/10.1175/1520-0442(2003)016%3C3706:SPAETA%3E2.0.CO;2).
- , and —, 2004: The flow of energy through the earth's climate system. *Quart. J. Roy. Meteor. Soc.*, **130**, 2677–2701, <https://doi.org/10.1256/qj.04.83>.
- , and Y. Zhang, 2019: Observed interhemispheric meridional heat transports and the role of the Indonesian Throughflow in the Pacific Ocean. *J. Climate*, **32**, 8523–8536, <https://doi.org/10.1175/JCLI-D-19-0465.1>.
- , J. T. Fasullo, and J. Kiehl, 2009: Earth's global energy budget. *Bull. Amer. Meteor. Soc.*, **90**, 311–324, <https://doi.org/10.1175/2008BAMS2634.1>.
- Ullrich, P. A., C. M. Zarzycki, E. E. McClenny, M. C. Pinheiro, A. M. Stansfield, and K. A. Reed, 2021: TempestExtremes v2.1: A community framework for feature detection, tracking, and analysis in large datasets. *Geosci. Model Dev.*, **14**, 5023–5048, <https://doi.org/10.5194/gmd-14-5023-2021>.
- Vonder Haar, T. H., and A. H. Oort, 1973: New estimate of annual poleward energy transport by Northern Hemisphere oceans. *J. Phys. Oceanogr.*, **3**, 169–172, [https://doi.org/10.1175/1520-0485\(1973\)003%3C0169:NEOAPE%3E2.0.CO;2](https://doi.org/10.1175/1520-0485(1973)003%3C0169:NEOAPE%3E2.0.CO;2).
- von Schuckmann, K., and Coauthors, 2016: An imperative to monitor Earth's energy imbalance. *Nat. Climate Change*, **6**, 138–144, <https://doi.org/10.1038/nclimate2876>.
- Walker, E., D. Mitchell, and W. Seviour, 2020: The numerous approaches to tracking extratropical cyclones and the challenges they present. *Weather*, **75**, 336–341, <https://doi.org/10.1002/wea.3861>.
- Yukimoto, S., N. Oshima, H. Kawai, M. Deushi, and T. Aizawa, 2022: Role of interhemispheric heat transport and global atmospheric cooling in multidecadal trends of northern hemisphere precipitation. *Geophys. Res. Lett.*, **49**, e2022GL100335, <https://doi.org/10.1029/2022GL100335>.